Energy Conversion and Management 243 (2021) 114341

Contents lists available at ScienceDirect

Energy Conversion and Management

journal homepage: www.elsevier.com/locate/enconman

A techno-economic analysis of solar catalytic chemical looping biomass refinery for sustainable production of high purity hydrogen

Baharak Sajjadi [a,*], Wei-Yin Chen [a], Maohong Fan [b], Asif Rony [b], Jennie Saxe [c], Jerzy Leszczynski [d], Tara K. Righetti [e]

[a] Chemical Engineering Department, University of Mississippi, 38677, United States
[b] Departments of Chemical and Petroleum Engineering, University of Wyoming 82071, United States
[c] Department of Civil and Environmental Engineering, University of Delaware, Newark, DE 19716, United States
[d] Interdisciplinary Center for Nanotoxicity, Department of Chemistry, Physics and Atmospheric Sciences, Jackson State University, Jackson, MS 39217, United States
[e] College of Law, University of Wyoming, Wyoming 82071, United States

ARTICLE INFO

Keywords:
Techno-Economic Analysis
Chemical Looping
Hydrogen
Pyrolysis
Gasification
Solar energy

ABSTRACT

Compared to traditional biomass and coal-fired power plants, a process that includes integrated pyrolysis and subsequent gasification is a promising technology to deliver a larger electrical output through the production of high-purity hydrogen with a low carbon footprint. Chemical looping can further enhance the biomass contribution to the global renewable energy demand while fulfilling the stringent CO_2 emission cuts needed in the energy sector. This study aims at investigating the feasibility of developing a solar catalytic chemical looping biomass refinery (SCCLBR) power plant for sustainable production of energy using a comprehensive plant modeling and techno-economic assessment. The plant is composed of 7 sequential units: i) biomass preparation (drying, transferring, and grinding), ii) reacting unit (SCCLBR), iii) water gas shift unit and heat recovery, iv) CO_2 and H_2S separation (Rectisol Process), v) sulfur removal (Claus Process), vi) air separation and vii) catalyst regeneration. The simulation was performed for 1–6 tonne/hour of biomass as input. The effect of key variables (feedstock load, water injection, and temperature) on the economic performance of the plant were analyzed. The simulated results of the chemical looping reactor were validated against the experimental results, while the results of Rectisol and air separation units were validated against the thermodynamic simulation. The results demonstrated that the CCLBR (without solar integration) and integrated SCCLBR can reach the efficiency of 34% and 41% respectively, yet the results have not been optimized. The sensitivity analysis indicated that water injection rate is the most influential parameter, which can even suppress the impact of biomass loading rate. A separate thermodynamic simulation was also performed to investigate the reaction equilibrium of oxygen carrier regeneration ($Ca_2Fe_2O_5$) using CO_2. The results demonstrated that a temperature above 730 °C is required to avoid carbonation (Fe_2O_3 and $CaCO_3$ production). The maximum greenhouse gas emission in SCCLBR is 10.70, which is significantly lower than traditional coal-to-hydrogen and biomass-to-hydrogen power plants. It has also been found that across varying feedstock input rates, greenhouse gas emissions average 12.8% lower when solar PV supplements refinery power needs; optimization of the steam/biomass ratio may reduce emissions even further.

1. Introduction

The global capacity of biomass plants totaled 140 GW in 2020. Biomass is currently the most widely used renewable energy source in the European Union (EU), representing about 90% of all renewable-based heating. However, according to 2020's statistical analysis, renewable energy provided only 11% of total energy consumption in the United States (US), 43% of which was supplied by biomass sources (EIA) [1]. On the other hand, the US and China possess the world's largest biomass power plant capacities at 16.2 and 17.8 GW, respectively [2]. The United States has abundant biomass resources (214.7 million metric dry tons), about 61.3% of which is corn stover [3]. Increasing the use of biomass and other renewable energy can contribute to reducing the United States' reliance on fossil fuels and combating climate change.

Pyrolysis and gasification are two promising technologies that

* Corresponding author.
E-mail address: bsajjadi@olemiss.edu (B. Sajjadi).

https://doi.org/10.1016/j.enconman.2021.114341
Received 15 February 2021; Accepted 20 May 2021

Nomenclature

A	Pre-exponential Factor (s^{-1})
A	Heat transfer area (m^2)
ASU	Air Separation Unit
Cp	Heat capacity at constant pressure (kJ $kmol^{-1}$ K^{-1})
C_{in}	Inlet concentrations ($kmol/m^3$)
C_{out}	Outlet concentrations ($kmol/m^3$)
CU	Claus Unit
CCL	Catalytic Chemical Looping
CellA	Intermediate Active cellulose
c_p	heat capacity (kcal/kg-°C)
D_c	Conveyor diameter (m)
$d_{p,}$	Particle diameter (m)
Ej	Activation energy of reaction j (kJ mol^{-1})
F	Volumetric flowrate (m^3/h)
ΔH	Enthalpy changes (kcal/h)
h	Enthalpy (kcal or kJ)
HTSR	high-temperature shift reaction
ΔH^0_f	Heat of formation of a feed stream (kJ $kmol^-$)
HMFU	5-hydroxymethyl-furfural
HAA	Hydroxyl-acethaldehyde ($C_2H_4O_2$)
H_{feed}	Feed enthalpy (kJ $kmol^{-1}$)
HP	High pressure
kW	Kilowatt
K	dimensionless number related to geometry
k,	specific heats (C_p/C_v)
k_{ij}	Binary interaction constant
k_H	Henry's constant
LOD	Loss on drying
LTSR	Low-temperature shift reaction
LP	Low pressure
LVG	Levoglucosan (1,2-anhydro-α-D-glucopyranose, C6H10O5)
L_c	Conveyor diameter (m)
L	Total liquid flow rate
LigH	Lignin Rich in Hydrogen ($C_{22}H_{28}O_9$)
LigO	Lignin Rich in Oxygen ($C_{20}H_{22}O_{10}$)
LigC	Lignin Rich in Carbon ($C_{15}H_{14}O_4$)
$\dot{m}_L$	Mass flow rate (kg/h)
MW	Megawatt
MeOH	Methanol
n	Tangential velocity distribution
nc	Number of components in the mixture
P	Power consumption (kW)
P	Pressures (Pa)
P_C	Critical pressure (Pa)
PSRK	Predictive SRK
Q_o	Operating throughput (m^3/h)
Q_s	Specific throughput ($m^3/h\text{-}m^2$)
Q	heat input or removal (kcal/h)
RU	Rectisol Unit
SRK	Soave–Redlich–Kwong equation of state
tonne	Metric Ton
T	Temperature (°C)
ΔT_{lm}	Log mean temperature difference (°C)
ΔT	Temperature change (°C)
T_C	Critical temperature (°C)
U	Heat transfer coefficient (kcal/h-°C-m^2)
V	Total vapor flow rate (m^3/h)
WGSR	Water gas shift reaction
WHB	Waste Heat Boiler
x_i	Mole fractions of component i in the liquid phase
y_i	Mole fractions of component i in the vapor phase
ψ	Dimensionless number related to operating conditions
$\rho_{p,}$	Particle density (g cm^{-3})
$\rho_{L,i}$	Pure component liquid densities (kg/m^3)
μ,	Gas viscosity (Pa.s)
u_T	Tangential particle velocity
η	Efficiency (%)
v_1	Volumetric throughput (m^3/h)
λ_i	Volumetric contribution coefficients
r_A	Combined reaction rate
ν	Stoichiometric coefficients
ω	Acentric factor

exploit energy from biomass. Pyrolysis is the thermochemical decomposition of biomass in the absence of oxygen to form a char and a gas and/or liquid that can be used to produce electricity or other fuels. In contrast, gasification is a thermal decomposition of biomass with the help of a gasifying agent to produce a gas (syngas). The gasification process comprises three main steps: moisture evaporation, devolatilization followed by homogeneous oxidation of the volatile matter, and heterogeneous oxidation of the char. Air, oxygen, and steam are the most widely used gasifying agents. Temperature, gasifying agent, feedstock type, size, inherent moisture content, and catalyst are among the most important parameters for estimating gasification effectiveness. In typical biomasses, the cellulose-to-lignin and hemicellulose-to-lignin ratios have the values of 0.5–2.7 and 0.5–2.0, respectively. Cellulose and hemicellulose yield gaseous products directly, while the lignin content is partially decomposed to oil. Therefore, a higher ratio of cellulose and hemicellulose to lignin yields a greater fraction of gaseous product. In terms of temperature effects, higher temperature (between 500 and 1400 °C) and faster heating rate lead to greater gas production and less tar production. Additionally, lower biomass particle size increases the conversion rate and product quantity. Smaller particles have higher heat transfer ability and more uniform temperature, which increases the gasification rate. Generally, a particle size of up to 0.15 mm is recommended for entrained flow gasifiers. Moreover, the gasifying agent affects the calorific value of the product gas. Although gasification is a proven technology for syngas production, optimization of the process and developing new technologies are still necessary to tackle the problems associated with energy production from biomass. Gasification demands a large amount of energy, particularly in the air separation unit.

Recent studies have demonstrated the possibility of H_2 enrichment through the integration of pyrolysis and inner-looping gasification. The concept of integrated pyrolysis and gasification has the purpose of shifting the reactions from exothermic to endothermic, which enhances the syngas yield and produces a high-quality gas: one with low tar content, higher hydrogen content, and subsequently greater heating value [4]. Additionally, the process consumes less energy compared with conventional gasification [5]. However, the process needs a bifunctional catalyst to simultaneously promote catalytic pyrolysis and gasification. Metal oxide composites have recently gained attention due to their low-cost and high (hydro) thermal stability. Fan et al [6] recently suggested that calcium ferrite catalyst composites (e.g. $Ca_2Fe_2O_5$) can increase H_2-rich gas production with tar abatement in steam-refinery of pinewood biomass. In integrated pyrolysis and gasification, CO and H_2 of syngas resulting from the steam-pyrolysis step reduce the $Ca_2Fe_2O_5$ to form CaO and Fe, while the catalyst can be oxidized (partially regenerated) during the steam gasification. As a result, gas production, tar cracking, and carbon conversion increased compared with the same process in the absence of $Ca_2Fe_2O_5$ catalyst. Imorb et al [7] evaluated the technical and economic performance of

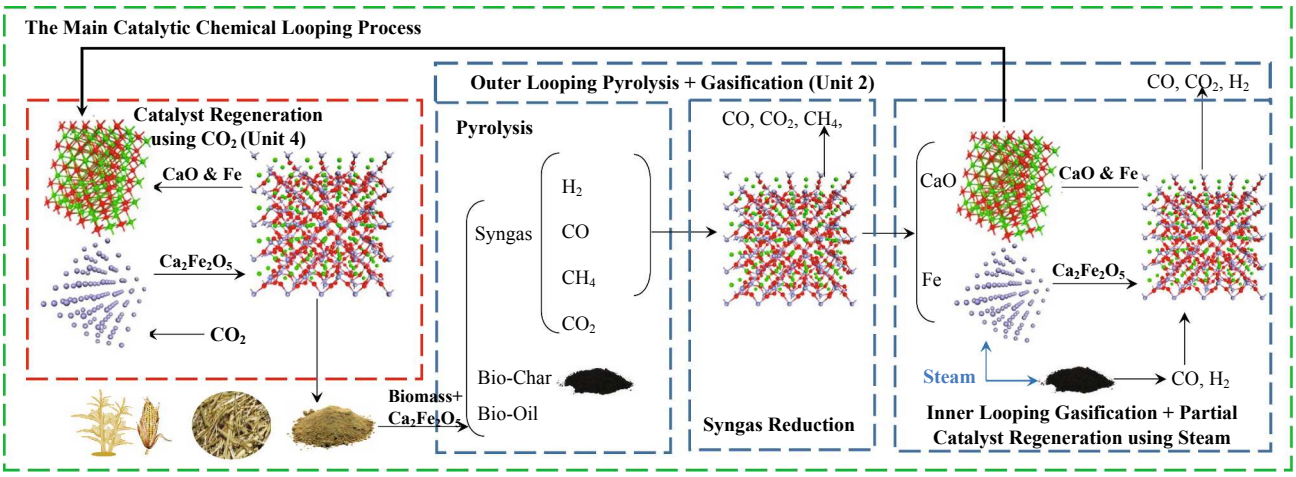

Fig. 1. A conceptual schematic diagram of chemical looping in SCCLBR (Adopted partially based on [6]).

integrated biomass pyrolysis and gasification for synthesis gas production from rice straw under different operating temperatures (400–700 °C) and concluded that 700 °C offers the best technical performance. Chai et al. [8] developed and studied a new catalyst Ni-CaO-C and evaluated its performance and CO_2 adsorption capability for integrated pyrolysis and gasification of plastics and biomass. Their experimental results indicated that high H_2 production (86.74 mol% and 115.33 mmol/g) and low CO_2 concentration (7.31 mol %) under the optimal operating conditions. Dai et al. [9] studied the integration of pyrolysis and entrained-bed gasification for the production of chemicals from Victorian brown coal. According to their results, the integrated process possesses an exergy efficiency 4.5% higher than the drying–gasification process. With a particular focus on lowering the gasification temperature and improving reactor design, Bartocci et al [10] investigated the hydrogen-rich gas production through integrated pyrolysis and steam gasification of the charcoal pellet. The process could reach hydrogen concentrations equal to 58.26% in volume. The results showed that the pyrolysis reaction could cover the entire heat required for the pyrolysis, reforming, and steam gasification stages.

On the other hand, the emerging concept of chemical looping (CL) refers to the decomposition of a chemical reaction into multiple sub reactions. The CL process typically involves the reduction and regeneration of an oxygen carrier (OC), such as metal oxides that can oxidize feedstocks. There are different types of CL processes such as chemical

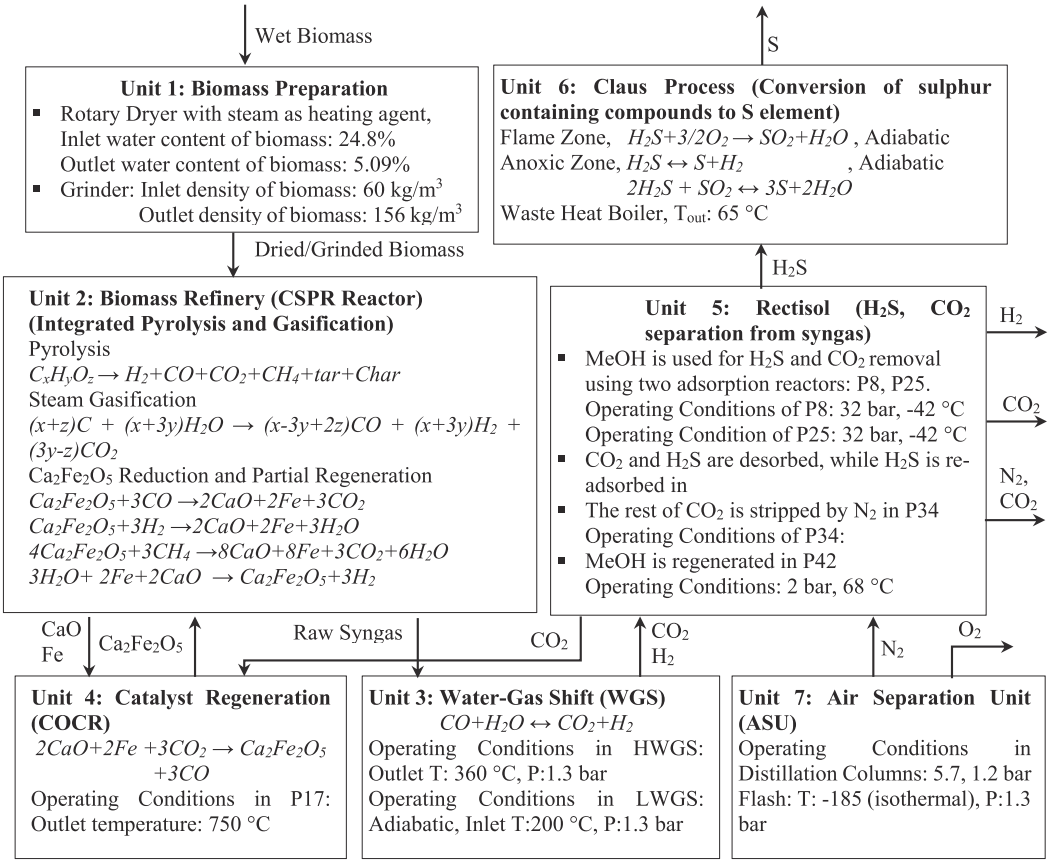

Fig. 2. Simplified process flow diagram of the SCCLBR representing the related reactions, model assumptions, performance indicators, and key parameters.

Table 1
The chemical characterization of pinewood and corn stover [53 54 55].

Content	Pinewood (wt%)	Corn Stover (wt%)
Cellulose	34.28	33.75
Hemicellulose	19.78	22.08
Lignin	19.97	12.99
Ethyl alcohol	0.71	0.71
Moisture	24.86	24.87
Sulfur	0.12	0.12
Ash	0.26	5.59

looping full oxidation, partial oxidation, thermochemical CO_2/H_2O splitting, selective oxidation, CO_2 capture, super-dry reforming, and desulfurization, among others. Chemical looping gasification is a particular case of partial oxidation, which aims at improving the yields of hydrogen production. This process has the potential to generate high quality syngas with lower CO_2 content and higher hydrogen production. This study integrates the two concepts of integrated pyrolysis/gasification with chemical looping in a (solar) catalytic chemical looping biomass refinery power plant (SCCLBR). $Ca_2Fe_2O_5$ was considered as the catalytic oxygen carrier (COC) of the CL process, the reduced form of which is re-oxidized and regenerated in the catalyst regeneration unit. Two different loops must be distinguished in this study. The first loop (outer looping) represents the biomass pyrolysis and the inner looping steam gasification along with partial regeneration of the catalyst using steam. This process occurs in one reactor (catalytic steam pyrolysis reactor, CSPR in biomass refinery unit). The second loop involves the complete regeneration of the reduced COC catalyst (CaO and Fe^0) using CO_2 (in catalyst regeneration unit) and the outer looping. In the overall process, the catalyst regenerator is the oxidation reactor, while the biomass refinery is the reducer reactor. A conceptual schematic diagram of these two loops has been provided in Fig. 1. The main objective the work focuses on assessing the feasibility and efficiency of establishing a full SCCLBR power plant based on the concepts of integrated pyrolysis/gasification with chemical looping using a comprehensive plant model. The entire process design, technical performance, and validation are presented in detail. The process includes seven units: i) biomass preparation, ii) reacting unit (SCCLBR) and heat recovery, iii) water gas shift unit, iv) CO_2 and H_2S separation unit (Rectisol), v) sulfur removal, vi) air separation unit (ASU) and vii) catalyst regeneration. Simulation of the process was performed using the SuperPro Designer package (Version 10) based on the experimental work on refinery reactor (half of the chemical looping process) done by our consortium at the University of Wyoming [6]. Rectisol and ASU units were separately simulated using PRO/II to ensure the accuracy of the economic analysis. While steam and oxygen are usually applied to re-oxidize the reduced catalyst, this study through the thermodynamic modelling proves, for the first time, that the reduced form of $Ca_2Fe_2O_5$ (CaO and Fe^0) can be re-oxidized and regenerated using CO_2. Therefore, a separate thermodynamic modelling was also performed to investigate the $Ca_2Fe_2O_5$ regeneration using CO_2.

2. Process Description and Simulation

A summary of the process modeled has been provided in Fig. 2. Each step in the process is detailed in the following sections.

2.1. Biomass Source

Biomass mainly consists of cellulose, hemicellulose, lignin, and moisture. The elemental composition of biomass is influenced by the environmental conditions, harvesting method, and elapsed time after harvest. For instance, corn stover biomass produced in the Northern US Corn Belt contains moisture at varying levels ranging from 47% to 66% [11]. Based on the 3-year average of the data presented in [12] 37% of the potential stover would be harvested at a range of moisture from 45% to 32%. On the other hand, according to the database for the physicochemical composition of (treated) lignocellulosic biomass [13] and a number of commercial lines [14] the moisture content of different biomass sources is between 24 and 25%. Accordingly, the average value of 24.87% moisture content was assumed for process simulation in this study and the rest of the components (e.g. cellulose, hemicellulose, and lignin) were normalized. Moreover, two different biomass sources including pinewood and corn stover were used for modeling the process. The characteristics of the biomass sources defined in the simulation were summarized in Table 1.

Table 2
Technical parameters used for the simulation of the power plant.

Item	Equipment	Parameter	Unit	Value
P-1	**Rotary Dryer**	Initial LOD- Final LOD	%	24.86–5.09
		Heating Agent-Temperature	-, °C	Steam, 242
		Specific Evaporation Rate	(kg/h)/m^3	20
		Outlet Gas T- Product T	°C	100
		Heat Transfer Efficiency [17]	%	70%
		Volatile Content of Outlet-Gas	wt/wt dry	0.02
P-2	**Screw Conveyer**	Shaft rotating rate	RPM	50
		Bulk Density of Conveyed Material [56]	kg/m^3	60
P-4	**Screw Conveyer**	Shaft rotating rate	RPM	50
		Bulk Density of Conveyed Material [57,58]	kg/m^3	156
P-5	**CCL Reactor**	Temperature	°C	750–850
		Pressure	bar	1.3
		Water	kg/h	200–560
P-72	**Tar Reformer**	Outlet Temperature	°C	700
		Pressure	bar	1.3
P-73	**H-WGS**	Outlet Temperature	°C	360
P-10	**L-WGS**	Adiabatic	–	–
P-8	**Absorption**	Thermal Equilibrium, Pressure	bar	32
P-25	**Absorption**	Thermal Equilibrium, Pressure	bar	32
P-39	**H_2S Concentrator**	Pressure	bar	3
		Top Stream Temperature	°C	−42
P-34	**Stripper**	Thermal Equilibrium, Pressure	bar	2
P-42	**Regenerator**	Pressure	bar	2
		Top Stream Temperature	°C	68
P-29	**Flash**	Adiabatic, Pressure	bar	7.5
P-30	**Flash**	Adiabatic, Pressure	bar	7.5
P-36	**Flash**	Adiabatic, Pressure	bar	1
P-50	**Flash**	Adiabatic, Pressure	bar	1.2
P-54	**Electric Heating**	Outlet Temperature	°C	600
P-60	**Electric Heating**	Outlet Temperature	°C	305
P-13	**Electric Heating**	Outlet Temperature	°C	250
P-55	**Flame Zone**	Adiabatic, Pressure	bar	1.3
P-53	**Anoxic Zone**	Adiabatic, Pressure	bar	1.3
P-81	**Distillation**	No. of Trays	–	45
		Pressure	bar	5.7
P-87	**Distillation**	No. of Trays	–	70
		Pressure	bar	1.2
P-85	**Flash**	Isothermal, Temperature	°C	−185
		Pressure	bar	1.3

2.2. Unit 1: Biomass Preparation Unit

2.2.1. Drying

There are over 100 distinct types of dryers commonly available which are categorized according to the particle size, uniformity of the input material, heating mode, as well as their capital and operating costs. The most common dryers are rotary dryers, belt dryers, flash

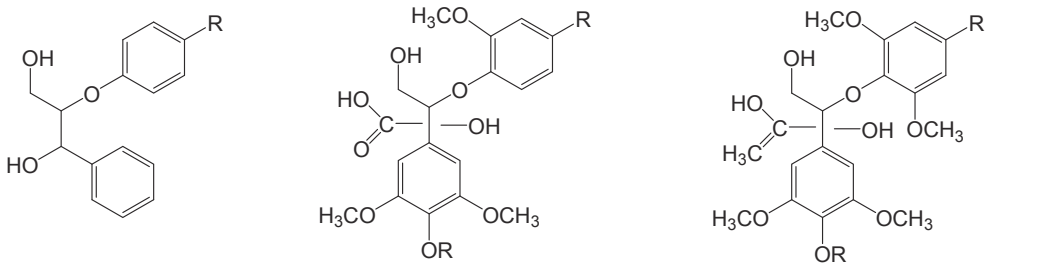

LIG-C ($C_{15}H_{14}O_4$) **LiG-O** $C_{16}H_{10}O_6(OCH_3)_4$ **LIG-H** $C_{17}H_{13}O_4(OCH_3)_5$

Fig. 3. Structure of different types of Lignin.

dryers, and fluidized-bed dryers. Rotary dryers are highly efficient options for solid bulks in large scale plants. These dryers are often chosen for their robust processing and uniform results. The rotary dryer consists of a large inclined rotating cylindrical drum with a diameter of 1–6 m, mounted on rollers and driven at a low speed. Heating can be applied either directly or indirectly. In direct heating, the hot air or gases pass through the material, while in an indirect configuration, hot gases in external tubes heat the material in an inner shell. Hot waste gases, flue gases, hot air, or flame (direct heating) could be the heat sources of dryers. Steam is another alternative that may be fed to a series of tubes inside the dryer's shell. Although the drying medium can flow in either co-current or counter-current of the material, the former is usually preferred for heat-sensitive materials. In this study, a rotary dryer with an indirect heating agent using high-pressure steam has been considered for the simulation. The details of the operating conditions have been summarized in Table 2 and its energy consumption has been validated against the commercial dryers [15–18].

2.2.2. Transferring

Screw conveyors are one of the most cost-effective devices for transporting bulk materials such as flakes, seeds, granules, grains, and powders. These devices can move non-flowing, wet, or caking materials that might otherwise be difficult to transport. Alternatively, they can be used to blend or mix materials. Screw conveyors consist of a helical screw element within a casing. They can work as independent mobile devices or as a part of other grain handling items such as dryers, feed mixers, distribution systems, etc. Screw conveyors normally have a diameter between 75 and 400 mm and a length of between 1 and 30 m [19]. In this study, two screw conveyors were modeled as summarized in table 2. The first one is a multi-step conveyor for transporting the initial biomass bulk and the second one is a one-step conveyor for transporting the ground and dried biomass powder. The power requirements, capacity, and volumetric efficiency of a screw conveyor are affected by the conveyor geometry, size, operating parameters and the properties of the material being conveyed [20]. The power requirements of the rotary conveyors of this study were calculated by considering the biomass particle size, density, shaft rotating rate as well as the number of conveyors needed in the multi-step one. The operating conditions were selected according to the commercial conveyors [20,21].

2.2.3. Grinding

Size reduction is one of the major pre-processing operations to produce the particle size needed. Grinders require considerable energy input (10–50 kW Mg-1) depending on the grinding mechanisms (impact, shear, attrition) and material [22]. The energy consumption by the grinder increases as the particle size decreases. Multiple-stage grinding is required in some processes. The main size reduction devices include disk chipper and drum chipper which reduce the size with replacement knives, producing clean edge/two-sided particles. Swing hammer hogs, fixed hammer hogs, and knife hogs are the other types of grinders that use swimming hammers, fixed hammers, and semi-sharp hammers respectively, to produce coarse/multi-surface particles and semi-coarse particles [23]. SuperPro Designer does not offer many different grinder options. In this study, a bulk grinder was modeled with a specific power consumption of 0.04 kW/(kg/h).

2.3. Unit 2: Biomass Refinery Unit

2.3.1. Integrated Pyrolysis-Gasification

The Solar Catalytic Chemical Looping Biomass Refinery (SCCLBR) in this study consists of two parts: a catalytic steam pyrolysis reactor (CSPR) and catalytic oxygen carrier regenerator (COCR). The first operational step in the SCCSPR involves the mixing of biomass particles with COC particles, followed by feeding the solid mixture into the CSPR. The CSPR is the outer-looping process that cycles between catalytic pyrolysis of biomass and inner-looping steam gasification of biochar. The primary pyrolysis kinetics and the corresponding heat of reactions used in this study as well as the details of the lignin structures were summarized in Table 2 and Fig. 3. Pyrolysis mainly includes 15 subsequent reactions in which biomass is decomposed into char, tar, and volatiles. The rest of the reactions in Table 3 include the secondary pyrolysis reactions for tar (Reactions 16–25), steam gasification (Reactions 29–31) as well as the tar generation from (lumped) phenol and its conversion (Reactions 32–37). Generally, an oxygen carrier is a type of metal oxide, which provides oxygen for fuel gasification. Iron-based oxygen carriers (OCs), such as Fe_2O_3, Fe_2O_3/Al_2O_3, and hematite, are the most widely used OC due to the low cost and environmental friendliness. However, the previous studies demonstrated that Fe-based OCs do not have enough reactivity, selectivity, and stability. Fe-contained composite oxides or those supported on La_2O_3, CeO_2, and Al_2O_3 have improved dispersion and alleviate the sintering problem. The selectivity of Fe-based OCs has also been further improved in $CaFe_2O_4$ and $BaFe_2O_4$, $Ca_2Fe_2O_5$, and $FeAl_2O_4$. These new composites had a low reactivity with synthesis gas in contrast to their great activity while reacting with solid fuel [24,25]. The technical and economic analysis of the catalyst consumption was validated against the experimental results. However, the lack of kinetic information related to the catalyst activity caused some deviation between the simulation results of the CSPR and the experimental results. Additionally, three different temperatures (from 750 to 850 °C) and water injection rates (from 0.08 to 0.235 steam/biomass weight ratio, dry basis) were considered. In real power plants, higher ratios of steam/biomass are usually applied (up to 0.5–1) to ensure the complete conversion of the reactions [26,27]. However, a number of reactions in the gasification process are reversible. Particularly, water gas shift reactions are severely affected by the amount of steam injected. On the other hand, Superpro designer assumes instant and perfect mixing of inlet streams with the compounds in the reactor. Therefore, any additional steam above stoichiometry may significantly affect the simulation results. In this study, the minimum quantity of steam has been considered for the simulation to ensure the validity of the results against the experimental ones.

2.3.2. Unit 4: Operation of COCR

The consumed catalyst can undergo a single-step oxidation regen-

Table 3
Primary pyrolysis reactions along with the reaction heat [59 60 61 62 63], [64 65], [66 67]

No.	Reactions	A(s^{-1})	E(kJ/mol)	ΔH($kJkg^{-1}$)
1.	Cell → CellA	8×10^{13}	192.5	447.7
2.	CellA → $5H_2O$ + 6Char	8×10^{7}	133.9	−1087.8
3.	CellA → Levoglucosan	4 T	41.8	732.2
4.	CellA → 0.95HAA + 0.25Glyoxal + 0.2Acetaldehyde + 0.25HMFU+0.2Acetone + $0.16CO_2$ + 0.23CO + 0·.$9H_2O$ + 0.1CH4 + 0.61Char	1×10^{9}	125.5	899.6
5.	HCell → 0.4HCell1 + 0.6HCell2	1×10^{10}	129.7	548.1
6.	HCell → $0.8CO_2$ + 0.675C + 1.4CO + 0.25 C_2H_4 + 0.125 EtOH + 0.5Formaldehyde + $0.75H_2$ + 0.625CH4 + 0.25 MeOH + 0.125Water	3×10^{9}	113	447.7
7.	HCell1 → Xylosan	3 T	46	707.1
8.	HCell2 → CO_2 + $0.5CH_4$ + $0.25C_2H_4$ + 0.8CO + $0.8H_2$ + 0.7 Formaldehyde + 0.25Methanol + 0.125 EtOH + 0·.$125H_2O$ + Char	1×10^{10}	138.1	259.4
9.	LigC → 0.35LigCC + 0.1pCoumaryl + 0.08Phenol + $0.41C_2H_4$ + H_2O+0.495CH4 + 1 H_2 + 1.32CO + 5.735Char	4×10^{15}	202.9	602.5
10.	LigH → LigOH + Acetone	2×10^{13}	156.9	523.0
11.	LigO → LigOH + CO_2	1×10^{9}	106.7	510.4
12.	LigCC → 0.3pCoumaryl + 0.2Phenol + 0.35Acrylic Acid + 0·.$7H_2O$+$0.65CH_4$ + $0.6C_2H_4$ + 1.8CO + H_2 + 6.4Char	5×10^{6}	131.8	288.7
13.	LigOH → Lig + H_2O + Methnaol + $0.45CH_4$ + $0.2C_2H_4$ + 2CO + $0.7H_2$ + 4.15Char	3×10^{8}	125.5	100.4
14.	4.5lig → $1C_6H_6O_2$(Resorcinol) + $3C_7H_8O_2$(Guaiacol) + $3C_8H_8O_3$(Vanillin)	8 T	50.2	577.4
15.	Lig → H_2O + 2CO + 0.2Formaldehyde + 0.4methanol + 0.2Acetaldehyde+0.2Acetone + $0.6CH_4$ + $0.65C_2H_4$ + $0.5H_2$ + 5.5Char	1.2×10^{9}	125.5	−205.2
16.	HMFU → 3CO + $1.5C_2H_4$	4.28×10^{6}	108.0	642.7
17.	Acetone → $0.5CO_2$ + $0.5H_2$ + $1.25C_2H_4$	4.28×10^{6}	108.0	1878.2
18.	pCoumaryl → CO_2 + $2.5C_2H_4$ + 3Char	4.28×10^{6}	108.0	−359.6
19.	Phenol → $0.5CO_2$ + $1.5C_2H_4$ + 2.5Char	4.28×10^{6}	108.0	−143.1
20.	Xylan → $2CO_2$ + H_2 + $1.5C_2H_4$	4.28×10^{6}	108.0	−563.0
21.	LVG → $2.5CO_2$ + $1.5H_2$ + $1.75C_2H_4$	4.28×10^{6}	108.0	1701.6
22.	HAA → 2CO + $2H_2$	4.28×10^{6}	108.0	3562.7
23.	Glycoxal → 2CO + $1H_2$	4.28×10^{6}	108.0	−156.6
24.	Acrylic-Acid → CO_2 + C_2H_4	4.28×10^{6}	108.0	−912.9
25.	Formaldehyde → CO + H_2	5×10^{11}	272	–
26.	C + CO_2 → 2CO	4364	248.12	–
27.	C + H_2O → CO + H_2	3.42 T		–
29	CH_4O → CO + $2H_2$	4.28×10^{6}	108	–
30	C_2H_4O + H_2O → 2CO + $3H_2$	4.28×10^{6}	108	–
31.	CO + H_2O ↔ CO_2 + H_2	7.68×10^{10}	304.624	−74.8
31.	Reversed Reaction	6.4×10^{9}	326.407	–
32.	C_6H_5OH(Phenol) → $1C_5H_6$ + 1CO	1×10^{11}	209	3295.8
33.	$2C_5H_6$ → $2H_2$ + $1C_{10}H_8$ (Naphthalene)	2×10^{7}	16.7	−268.0
34.	$2C_6H_6O_2$ (Resorcinol) → $1C_{10}H_8$ + $2CO_2$ + $2H_2$	5.01×10^{14}	310,871	2646.3
35.	$C_8H_8O_3$ (Vanillin) + H_2 → C_7H_8O + 1CO + H_2O	1.3×10^{11}	175.309	−1956.9
36.	C_7H_8O (Anisole) + $2H_2$ → C_6H_5OH + H_2O	7.94×10^{10}	226.354	−1062.7
37.	$C_7H_8O_2$ (Guaiacol) + $2H_2$ → C_6H_5OH + CH4 + H_2O	1.58×10^{12}	191.000	−720.6

eration, as below:

$$2CaO(s) + 2Fe(s) + 3CO_2(g) \leftrightarrow Ca_2Fe_2O_5(s) + 3CO(g) \Delta H^{\circ}_{1123} = -7.05 kjmol^{-1}$$

In the COCR reactor, CO_2 is added to react with and regenerate spent COC. The O in CO_2 is used to replenish the O in spent COC. The regenerated COC particles are then separated from the outlet gas stream via another cyclone unit. The regenerated COC particles with severe coke deposition are recycled back to the COCR for carbon removal or further regeneration, whereas the COC particles with much less carbon deposition are returned to the CSPR, leading to the termination of one chemical looping. A cyclone directly connected to the CSPR is used to separate the gas mixture from biochar, unreacted biomass, and oxygen-depleted COC. The unreacted biomass discharged at the bottom of the cyclone can then recycled back to the SCSPR; whereas, the spent COC and biochar are carried to an auxiliary cyclone unit for further separation. At the outlet of this unit, the spent COC is transferred to the COCR for regeneration.

2.3.2.1. Particulate Removal Using Cyclone Separator. The product gas stream from the gasifier contains a significant level of particulates and tar, which are problematic if not handled properly. The particulates consist of unconverted char, ash, and bed material (e.g. catalysts). Deposition of particulates in the downstream equipment causes plugging and increases the maintenance costs. Cyclone separators have routinely and widely been used to separate the particulate impurities above 5 ~ 10 μm in diameter from the gas stream. Separation in a cyclone is achieved by utilizing inertial forces. Smaller particulates can be further removed using wet scrubbers, various barrier filters, and electrostatic precipitators. In a typical cyclone, the incoming flow is forced to rotate, while it simultaneously moves down due to gravity. The shrinkage cross-section of the bottom of the cone generates a reverse flow pulling the flow (light components e.g. gas) upward. The performance of the cyclone is generally affected by the cyclone dimensions, the particle properties, and the operating conditions [28]. In industrial scales, multiple cyclones are usually used to increase separation efficiency. In this study, the effect of three cyclones on the gas stream was modeled. The first one (P-23) was used to separate ash and unreacted carbon, which are usually accumulated at the bottom of the reactor. The second cyclone (P-6) was used for the separation of consumed COC and the third one (P-14) was used to boost the impact of the other two cyclones in the separation of trace amount of ash and carbon from the

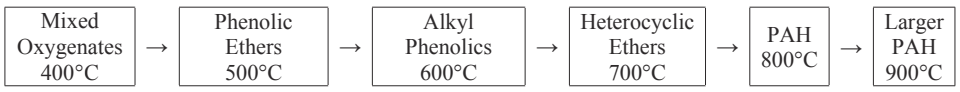

Fig. 4. "Tar" maturation scheme proposed by Elliot (1988) [31].

Table 4
Kinetic Parameters of tar cracking and steam reforming, [64 68]

No.	Reactions	Reaction rate
38	$C_{10}H_8 + 4H_2O \rightarrow C_6H_6 + 4CO + 5H_2$	$r = 1 \times 10^{11} \exp(-324.000/RT)\ [C10H_8]\ [H_2]^{0.4}$
39	$C_6H_6 + 5H_2O \rightarrow 5CO + 6H_2 + CH_4$	$r = 4.4 \times 10^{5} \exp(-220.000/RT)\ [C6H_6]$
40	$CH_4 + H_2O \rightarrow CO + 3H_2$	$r = 3.0 \times 10^{5} \exp(-15.042/T)[CH_4]\ [H_2O]$
41	$C_2H_4 + 2H_2O \rightarrow 2CO + 4H_2$	$r = 3100.0 \exp(-15.000/T)[C2H_4]\ [H_2O]^2$
42	$C_2H_6O + H_2O \rightarrow 2CO + 4H_2$	$r = 4.28 \times 10^{6} \exp(-108/RT)\ [C_2H_6O]\ [H_2O]$

consumed COC. The operating conditions and cyclone performance have been defined and validated according to the industrial ones [29,30].

2.3.3. Steam Reforming of Biomass Tar

One of the main problems of biomass gasification is that the produced gas usually contains amounts of highly viscous impurities, which are known as "tar". These compounds comprise a mixture of single- to five-ring aromatics, some oxygen-containing hydrocarbons, and complex polycyclic aromatic hydrocarbons (PAH) which are produced during thermal decomposition of biomass, mainly lignin. According to Elliott's scheme [31] the chemical structure of tars can be classified as per their gasification or pyrolysis temperatures (Fig. 4). Tar compounds can be divided into three groups of primary, secondary and tertiary, which are produced in temperatures ranging between 400 and 700 °C, 700–850 °C, and 850–1000 °C, respectively [32]. The stability of tar compounds increases with gasification temperature. Based on molecular weight, tars can also be divided into 5 classes: Class 1) not detectable by GC; Class 2) Heterocyclic aromatic compounds which are water-soluble; Class 3) Light hydrocarbon aromatic compounds (1 ring); Class 4) Light polyaromatic hydrocarbon compounds (2–3 rings), and Class 5) Heavy polyaromatic hydrocarbon compounds (4–7 rings) [32]. In this study, a high temperature (750–900 °C) is applied, resulting in secondary and tertiary tars (mainly tertiary), including PAH with 2–3 rings and heavy PAH with 4–7 rings, as the most probable produced tars. The kinetic parameters for the tar generation from (lumped) phenol used for simulation of tar compounds formation were summarized in Table 2 (reactions 32–37). Tars are condensable and can block pores either in the condensed or cracked form (or coke), and cause fouling corrosion, abrasion, and erosion of process equipment. Generally, tars can be removed through physical non-catalytic processes (e.g. thermal cracking) or chemical catalytic conversions; among which the latter is more economical due to the decomposition of tar compounds to fuel gases (e.g. H_2, CO, CH_4) at a lower temperature compared with non-catalytic tar conversion. Catalytic tar conversion can be accomplished through two methods: 1) mixing catalyst with the feed biomass prior to gasification or 2) catalytic elimination of the produced tars in a secondary reactor after gasification. Minerals (e.g. calcined rocks, olivine, clay minerals, and ferrous metal oxides) and synthetic compounds (e.g. char, FCC Catalysts, alkali metal carbonates, and transition metals-based) are the two main categories of the catalyst used in the catalytic conversion of tars. Minerals exist naturally and can be used directly or with slight modification and hence they are relatively cheap [33]. Among different tar elimination methods, catalytic steam reforming has been widely used since the presence of a catalyst can effectively convert tar into fuel gas and the presence of steam assists the process in producing lighter molecules such as H_2 and CO. Accordingly, steam reforming was selected for tar removal in the current study (Table 4).

Table 5
WGS reaction rate with high (HTSR) and low temperature (LTSR) catalysts, [69,70].

No.	Reactions	Re	A(s^{-1})	E(kJ/mol)	ΔH(kj/g)
43	$CO + H_2O \rightarrow CO_2 + H_2$	HTSR	7.39	75	−1.46
44	$CO_2 + H_2 \rightarrow CO + H_2O$	HTSR	33	75	1.46
45	$CO + H_2O \rightarrow CO_2 + H_2$	LTSR	2.96×10^5	47.4	−1.46
46	$CO_2 + H_2 \rightarrow CO + H_2O$	LTSR	1.409×10^3	47.4	1.46

2.3.4. Heat Recovery

The syngas leaving the gasifier or CSPR (herein) and the subsequent tar removal reactor has a high temperature (sometimes up to 1600 °C). Hence, all plants require cooling or a heat recovery system after the gasifier or CSPR (herein) and before the cleaning systems (e.g. scrubber and the sulphur removal system), which usually operate at temperatures remarkably lower than that of the gasifier. This task is accomplished by using a heat exchanger (also known as syngas cooler), which transfers the heat of the syngas to the cooling medium, converting water into high pressure, high-temperature steam. Heat recovery can improve process efficiency by approximately 5% and can reclaim a remarkable portion (5–25%) of the energy in the feed. The syngas can be cooled by a radiant cooler, convective cooler, or direct quench system. A radiant syngas cooler (RSC) includes a tube cage comprising a plurality of tubes and a vessel shell defining an interior region for cooling of syngas. Heat is exchanged from the hot syngas (greater than700–1650 °C) at an interior region to the water that flows in tubes through radiant heat transfer. As a result, high-pressure (HP) steam is generated. There is a slag quench chamber at the bottom of the RSC, which collects and removes the cooled molten slag. Convective syngas coolers (CSC) comprise a container (shell) and set of tubes inside the container. CSC is usually used to recover heat from gas at a temperature around or below 1000 °C. CSC uses convection and conduction to cool the hot syngas in the tubes and produce high or intermediate pressure (IP) steam (between 10 and 15 MPa) in the shell. Quenching is the fastest technique for cooling the syngas. In direct quench coolers, a cooling medium is directly injected into the syngas. The cooling medium could be water, cooled syngas, or chemical quench cooling. Water injection into the quench system imposes the water gas shift reaction, increasing H_2 production and the efficiency of the system. The addition of chemical quench has not been widely applied in industry. However, on the other hand, there is no heat recovery in the quench cooling process. In other words, the significant heat of the hot syngas is converted to low-level process heat rather than high-pressure steam [34]. In this study, two subsequent heat exchangers were simulated to recover the syngas heat to produce high pressure, high-temperature steam, which was recycled to the biomass refinery reactor.

2.4. Unit 3: Water Gas Shift Unit

The main purpose of the water gas shift reaction (WGSR) is to convert the CO in the product syngas to CO_2, while the steam used in the process further increases the hydrogen content of the final product. Hence, the water gas shift reaction enriches the CO_2 and H_2 in the processed gas. WGSR is a moderately exothermic equilibrium-limited reaction, which is kinetically favored at high temperatures and thermodynamically favored at low temperatures. To maximize the CO

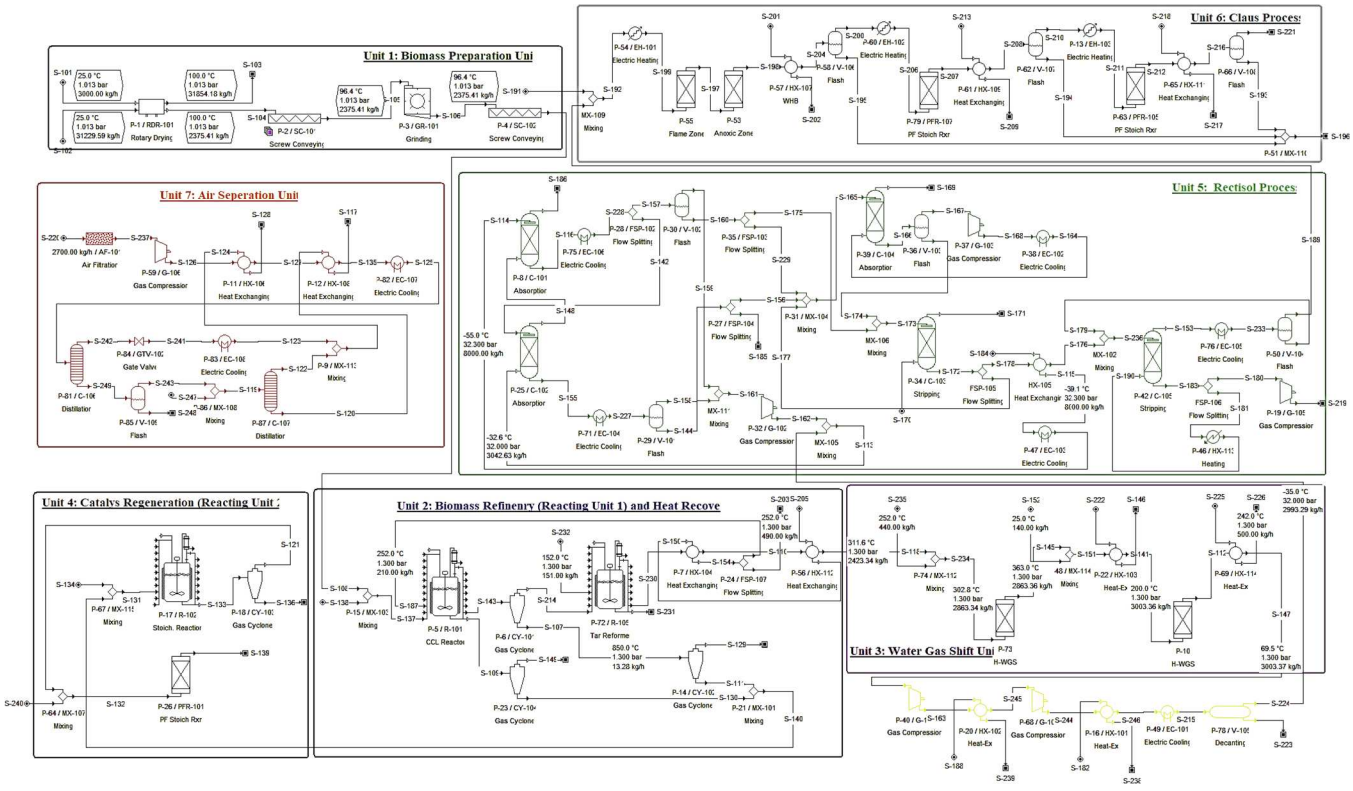

Fig. 5. Simulation configuration of solar catalytic chemical looping biomass refinery (SCCLBR) power plant using SuperPro Designer.

conversions and reaction rates and subsequently H_2-enriched biogas, WGSR typically occurs in two adiabatic reactors, with cooling between them. The first reactor consists of a high-temperature shift section (HTSR at 320–360 °C) with an iron-based catalyst, while the second one is a low-temperature shift converter (LTSR at 190–250 °C), using a copper-based material. The reactions and kinetics used in this study for the two-step WGS reactors were summarized in Table 5.

2.5. Unit 5: CO_2 and H_2S Removal Unit based on Rectisol Technology

Rectisol is one of the leading processes concerned with selective removal of H_2S and CO_2 from any raw syngas while preserving the H_2

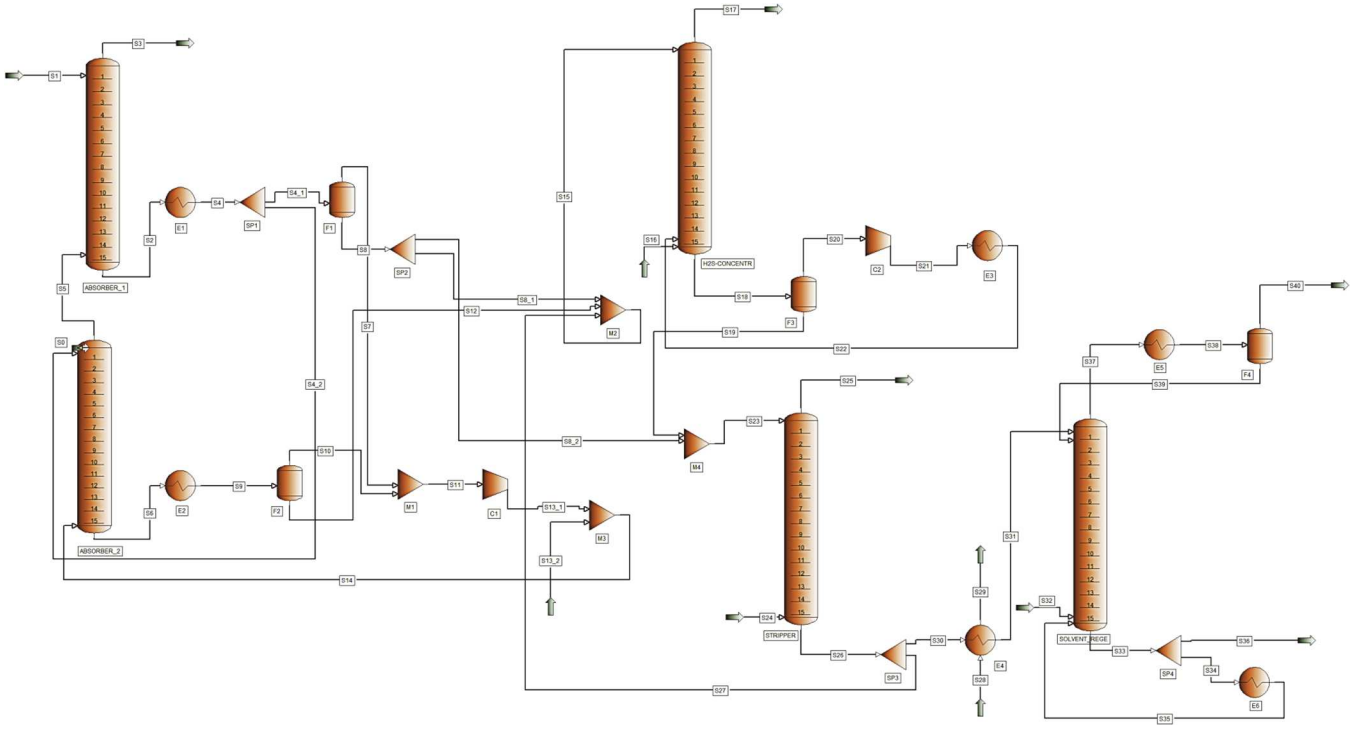

Fig. 6. Simulation configuration of the Rectisol process for CO_2 capture using PRO/II.

Table 6
WGS reaction Rate with high and low temperature catalysts [71–73 74,75 37,75]

No.	Reactions	Re	A(s^{-1})	E(kJ/mol)	ΔH(kj/g)
47	$H_2S + 1.5O_2 \rightarrow SO_2 + H_2O$	Flame Zone	14×10^4	46,024	−15.23
48	$H_2S \rightarrow H_2 + S$	Anoxic Zone	5.263×10^6	188,280	3.109
49	$H_2 + S \rightarrow H_2S$	Anoxic Zone	13.6×10^3	97,905	−3.109
50	$2H_2S + SO_2 \rightarrow 3S + 2H_2O$	Anoxic Zone	1.57×10^7	208,781	1.364
51	$3S + H_2O \rightarrow 2H_2S + SO_2$	Anoxic Zone	5×10^5	187,861	−1.364
52	$2H_2S + SO_2 \rightarrow 3S + 2H_2O$	Catalytic Reactor	Conversion Factor		

and CO. Rectisol is a tight integration of absorption/desorption with significant pressure and temperature variations. In Rectisol process, cold methanol is used as a solvent to physically absorb acid gas components from the syngas. The main advantages of the process are the use of an inexpensive and easily available solvent, generation of high purity syngas, and flexibility in process configuration. However, Rectisol can be quite expensive due to the required refrigeration to reduce the temperature of methanol to −40 °C to −62 °C.

The Rectisol process simulated in this study is the adapted version of the process originally developed and patented by Lurgi and Linde [35,36]. The process is composed of four main blocks: i) two acid gas absorbers, ii) H_2S concentrator (CO_2 desorber), iii) CO_2 stripper, and iv) solvent regenerator. The process starts with two absorption columns in which two chilled methanol streams at 223 and 213 K wash the CO_2, H_2S, and carbonyl sulfide (COS) out from the syngas. The bottom column captures all H_2S essentially because its solubility into methanol is significantly larger than that of CO_2. Hence, CO_2 is partially captured in the bottom column and the rest of the CO_2 is captured in the upper column. The next block consists of the flash of the CO_2-loaded methanol, which releases almost all CO_2 and partially releases H_2S by lowering the pressure, and an absorber column that re-absorbs the H_2S, resulting in the enrichment of MeOH with H_2S. The remaining fraction of CO_2 in the H_2S-enriched methanol stream is then stripped with nitrogen in the acid gas stripper. A mixture of N_2 and CO_2 is extracted at the top of the stripper. Finally, the H_2S-enriched methanol is fed into the regeneration tower, where H_2S and any remaining CO_2 are removed from the solvent through cooling and flashing. Methanol is recycled to the top of the column, combined with additional MeOH, heated, and recycled to the bottom of the regenerator. The flow diagram of the Rectisol process simulated using SuperPro Designer (unit 5) and Pro II have been presented in Figs. 5 and 6, respectively.

2.6. Unit 6: Sulfur Recovery Unit based on Claus Technology

The acid gas produced by the solvent regenerator (from Rectisol Process) contains large amounts of sulfur components (e.g. H_2S) which cannot be emitted to the atmosphere. Among a broad number of processes that could be implemented for sulfur recovery, the Claus process is applicable for feeds containing a high amount of H_2S (greater than 30 mol %). The Claus process is composed of one thermal stage and two catalytic stages. In the thermal stage, the H_2S-laden gas is preheated and burned with air or oxygen. The thermal stage consists of three zones: the flame zone, anoxic zone and Waste Heat Boiler (WHB). H_2S is a combustible gas. In the flame zone, which is typically adiabatic, H_2S is combusted to form sulfur dioxide($H_2S + 3/2O_2 \rightarrow SO_2 + H_2O$) with a desired stoichiometric ratio of2:1 H_2S to SO_2. The gas then passes through the anoxic zone, where a wide range of reactions may occur depending on the gas composition, the most important of which result in sulfur formation (Reactions 48–51). The flame and anoxic zones both happen in different zones of a single furnace, however, they are separately modeled as adiabatic plug flow reactors. As the hot furnace exhaust (926–1300 °C) is cooled in the WHB (to 230–370 °C), middle-pressure steam is produced, while elemental sulfur is condensed and removed from the gases. Usually, about 60–70% of the total elemental sulfur is produced in the thermal stage [37]. The outlet stream of WHB passes through two catalytic processes, either of which consists of heating, catalytic reaction, cooling and condensation. The reactions and kinetics used in this study for the Claus process were summarized in Table 6.

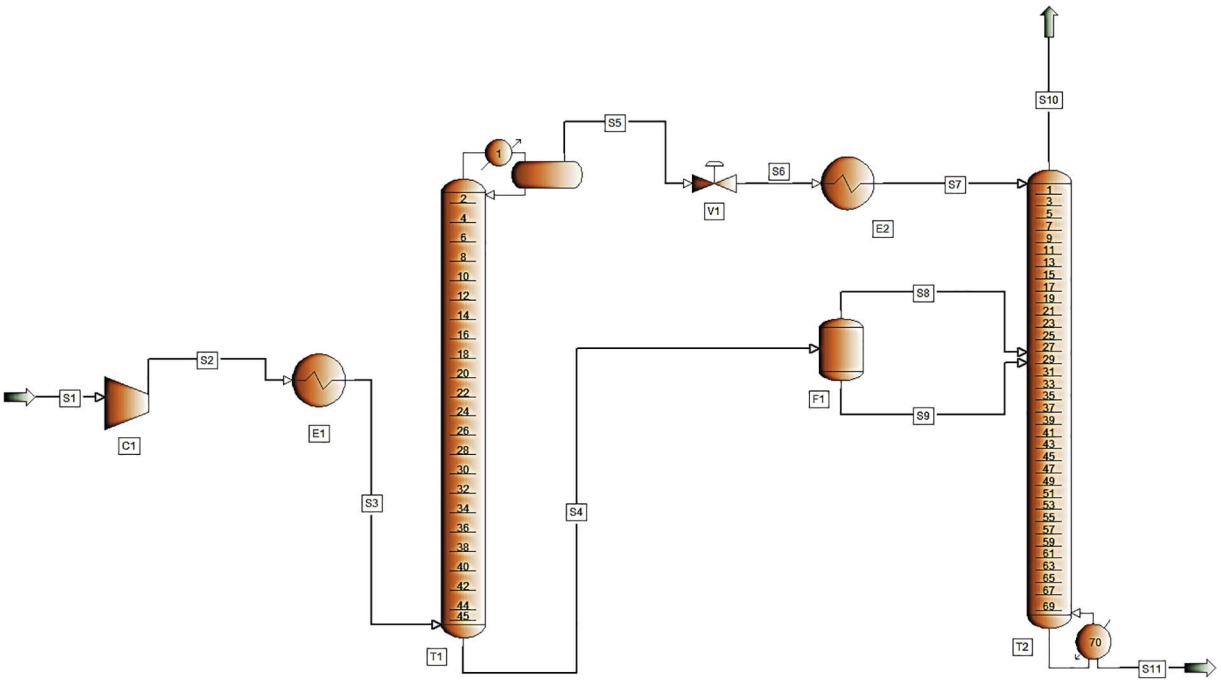

Fig. 7. Simulation configuration of the Air Separation process for using PRO/II.

2.7. Unit 7: Air Separation Unit

The technologies to separate oxygen from air are categorized into cryogenic and non-cryogenic methods. The non-cryogenic air separations are mainly applied through adsorption or membrane-based methods. Adsorption of nitrogen from the air at the surface of beds (e.g. zeolite) is among the most widely used methods. The process runs cyclically between two adsorption columns (in on and off modes). When the adsorbent bed is saturated, the column mode is switched to off-mode and regeneration takes place by reducing the pressure (pressure swing adsorption). High purity oxygen (95%) can be obtained in this method. In cryogenic methods, separation takes place by the use of differences in condensation temperatures of particular gases in rectifying columns. In this process, pre-cooling (to −200 °C) and compression steps are applied to liquefy and condense air and overcome pressure drops during gas flows. Water vapor condenses and is removed using absorbent filters. Carbon dioxide freezes at –79 °C and is removed by a molecular sieve. The liquid nitrogen (liquefied at −196 °C) and oxygen (liquefied at −183 °C) are then separated by fractional distillation. The oxygen-enriched stream is then subjected to another step for the removal of argon. The oxygen product purity in this method usually ranges from 97.5 to 99.5%. The flow diagram of the cryogenic process simulated using SuperPro Designer (unit 7) and Pro II have been presented in Figs. 5 and 7, respectively.

The simulation configuration of the solar catalytic chemical looping biomass refinery (SCCLBR) power plant is presented in Fig. 5.

2.8. Mathematical Modeling

2.8.1. Rotary Drying

The evaporation calculations are based on the liquid/solid portion of the wet feed stream only. A two-phase modeling was assumed in which the dried product (final solids) stream appears entirely in the liquid phase and that the outlet drying gas stream appears entirely in the gaseous phase. The component material balances were done based on the evaporation percentages of pure steam that is set as volatile. The evaporation percentage was calculated based on the specified 'Final loss on drying (LOD)' value. A stream's LOD is calculated as below:

$$\mathrm{LOD} = \frac{\dot{m}_L}{\dot{m}_{L,S}} \tag{1}$$

where $\dot{m}_L$ (in kg/h), and $\dot{m}_{L,S}$ (in kg/h) denote the total liquid mass flow rate and total liquid/solid mass flow rate, respectively. The 'Initial LOD' ($\mathrm{LOD_i}$: the LOD of the wet feed stream) is first determined by dividing the total liquid mass flow rate of the wet feed stream by the total liquid/solid mass flow rate of that stream. The 'Final LOD' ($\mathrm{LOD_f}$) was specified according to the literature, and the evaporation percentage (E) was calculated using eq (2).

$$\mathrm{E} = 100 \times \frac{(\mathrm{LOD}_I - \mathrm{LOD}_F)}{\mathrm{LOD}_I/(1 - \mathrm{LOD}_F)} \tag{2}$$

In this work, air and steam were considered as the drying gas and heating agent. Therefore, the following energy balance was solved to calculate the heating duty ($\dot{\mathrm{Q}}$) and the mass flow rate of the heating agent ($\dot{\mathrm{m}}_A$):

$$\sum\left(h_{\mathrm{A,i}} + h_{\mathrm{f,i}} + \dot{\mathrm{Q}}\right) = \sum\left(h_{\mathrm{A,o}} + h_{\mathrm{P,o}}\right) \tag{3}$$

$$\dot{\mathrm{m}}_A = \eta \times \frac{\dot{\mathrm{Q}}}{\alpha_A} \tag{4}$$

where $h_{A,i}$, $h_{f,i}$, $h_{A,o}$, $h_{P,o}$ denote the enthalpy of the inlet drying gas stream, wet feed stream, and outlet drying gas stream, outlet dried product stream, respectively. η and α_A denote the efficiency and the heating agent's mass-to-energy factor. The dew point of the outlet gas stream was calculated by flashing the outlet gas stream based on the assumption that Raoult's law is applicable to all volatile components contained in it. The operating pressure in the dryer was assumed to be equal to the minimum pressure of the two inlet streams (wet feed and inlet drying gas).

2.8.2. Screw Conveyors and Grinder

Equipment size and power consumption are the key parameters for the screw conveyor. The bulk density of the conveyed material was used to convert the mass throughput into volumetric throughput. The conveyor diameter was calculated by dividing the operating throughput (m^3/h) by the specific throughput (m^3/h-m^2). Since the calculated diameter of the first conveyor (SC-101) exceeded the maximum allowed, two identical units were considered for this step, operating in parallel with a total cross-sectional area equal to the calculated. To account for electricity consumption, the specific power requirement (P_s in W/(m^3-h)-m) was specified according to the literature and similar industrial conveyors. Accordingly, conveyor diameter (D_c) and total power consumption (P) were calculated using the below equations:

$$D_C = \frac{Q_O}{Q_S} \tag{5}$$

$$P = P_s \times Q_O \times L_C \tag{6}$$

where, D_c (m), L_c (m), Q_o (m^3/h), and Q_s (m^3/h-m^2) denote the conveyor diameter, conveyor length, operating throughput, and specific throughput.

Similar to the screw conveyor, the power consumption of the grinder (in kW/kg-h) was calculated based on the specific power requirement and the operating throughput:

$$P = P_s \times Q_O \tag{7}$$

2.8.3. Cyclones

The overall removal efficiency of the cyclone is the sum of the products of the removal efficiency for each particle size (η) times the weight fraction of that particle size.

$$\eta = 100 \times \left[1 - exp\left(-2(C\psi)^{1/(2n+2)}\right)\right] \tag{8}$$

$$C = \frac{8K_c}{K_a K_b} \tag{9}$$

$$\psi = \frac{d_p^2 \rho_P u_T (n+1)}{18\mu D} \tag{10}$$

where, C and ψ are dimensionless numbers related to cyclone design and operating conditions. In these two equations, K_c , K_a and K_b are the dimensionless numbers related to the volume, body diameter and height and ρ_p, d_p, μ, n and u_T are the particle density, particle diameter, gas viscosity, the dimensionless exponent of the vortex law for tangential velocity distribution and the tangential particle velocity, respectively. Tangential particle velocity is calculated through ($u_T = \frac{Q}{ab}$), where Q is the volumetric flowrate of the gas through the cyclone.

2.8.4. Heat Exchangers and Electrical Heaters/Coolers

The energy balance in heat exchangers the heat transfer (exchange) rate, Q (kcal/h), were modeled through equation (11):

$$Q = \eta U A \Delta T_{lm} = \Delta H_{hot} = \Delta H_{cold} \tag{11}$$

where, η, U(kcal/h-°C-m^2), A (m^2), ΔT_{lm} (°C), m (kg/h), c_p (kcal/kg-°C) are the correction factor that accounts for deviations from counter-current or co-current flow, overall heat transfer coefficient, heat transfer area, log mean temperature difference in the system, mass flowrate of the stream and specific heat capacity of the stream, respectively. ΔH_{hot}

and ΔH_{cold} (kcal/h) are the enthalpy changes of the hot and cold streams.

The heating and cooling in the electrical heaters and coolers are achieved using electricity. The following equation was used to calculate the energy balances (electric power, kW) of such equipment:

$$P = mc_p\Delta T/\eta \tag{12}$$

where, m (kg/h), c_p (kcal/kg-°C), and ΔT(°C) represent the mass flowrate of the stream, the specific heat capacity of the stream, and the temperature change of the stream. η is the heat transfer efficiency in electrical heating, also referred to as the coefficient of performance (the ratio of cooling load to electricity consumption) in electrical cooling.

2.8.5. Gas Compressors

The physical operation of the compressors falls between the isentropic and isothermal extremes. This equipment often needs external cooling to prevent significant increase in the temperature of the compressed fluid. To calculate the power and cooling requirement of the actual process, an isentropic process is assumed first followed by calculation of the outlet temperature and the energy required to reduce the temperature to a desired value.

$$Power = \frac{k}{k-1}P_1V_1\left[\left(\frac{P_2}{P_1}\right)^{(k-1)/k} - 1\right] \tag{13}$$

In eq (13), k, v_1, p_1, and p_2 are the ratio of specific heats (C_p/C_v), volumetric throughput of gas at the inlet, the inlet, and outlet pressures, respectively. To calculate the outlet temperature for an isentropic process, the below equation was used:

$$T_2 = T_1\left(\frac{P_2}{P_1}\right)^{(k-1)/k} \tag{14}$$

where, T_1 and T_2 denote the inlet and outlet temperatures of gas.

2.8.6. Distillation Columns

To simulate the distillation columns, a set of constitutive relationships were applied to each stage. The equations represent the total mass balance, component mass balance, energy balance, equilibrium relationship, continuity equation and thermodynamic models, respectively:

$$F_n + V_{n+1} + L_{n-1} = V_n + L_n \tag{15}$$

$$F_n z_n + V_{n+1}y_{n+1} + L_{n-1}x_{n-1} = V_n y_n + L_n x_n \tag{16}$$

$$Q_n^{external} + F_n h_{f,n} + V_{n+1}h_{V,n+1} + L_{n-1}h_{L,n-1} = V_n h_{V,n} + L_n h_{L,n} \tag{17}$$

$$y_n = Kx_n \tag{18}$$

$$\sum_i x_i - \sum_i y_i = 0 \tag{19}$$

$$K = f(P, T, x_i, y_i) \tag{20}$$

$$h = f(P, T, z_i, phase) \tag{21}$$

where, y_i and x_i are the mole fractions of the i-th component in the vapor and liquid phases, respectively. F, L and V are the total feed, liquid and vapor flow rates; h, and Q represent the enthalpy and heat input or removal.

2.8.7. Flash drums

The thermodynamic equilibrium imposes equal vapor and liquid phase temperature and pressure in the flash drums. Accordingly, the single-stage flash was modeled using the following equations, representing the total mass balance (eq. (22)), phase equilibrium (eq. (23)), summation constraint (eq. (24)), energy balance (eq. (25)), respectively.

$$F = V + L \tag{22}$$

$$y_i = K_i x_i \tag{23}$$

$$\sum_{i=1}^{nc}(y_i - x_i) = 0 \tag{24}$$

$$h_F F + Q = h_V V + h_L L \tag{25}$$

where F, V, L and y_i, x_i denote the molar flowrates of the feed, vapor and liquid stream, and the molar fraction of component *i* in gas and liquid streams, respectively. The density of the vapor mixture was calculated using the ideal gas assumption (Z = 1). The ideal mixture model was also used for calculating the density of the liquid mixture.

$$\widehat{\rho}_V = \frac{P}{ZRT} \tag{26}$$

$$\widehat{\rho}_L = \frac{\widehat{m}_L}{\widehat{V}_L} = \frac{\sum_{i=1}^{nc} m_i}{\sum_{i=1}^{nc}\lambda_i\frac{m_i}{\rho_{L,i}}} \tag{27}$$

where *nc* , λ_i and $\rho_{L,i}$ denote number of components in the mixture, volumetric contribution coefficients and the pure component liquid densities, respectively. In addition, the heat capacity, enthalpy and partial fugacity of the vapor phase were calculated under the ideal mixture assumption using the below equations:

$$\widehat{c}_p^V = \sum_{i=1}^{nc} y_i c_{p,i}^V \tag{28}$$

$$\widehat{h}_v(T) = \sum_{i=1}^{nc} y_i h_{v,i}(T) \tag{29}$$

$$\widehat{f}_{v,i} = \widehat{\varphi}_{V,i} y_i P \tag{30}$$

$$ln\left(\widehat{\varphi}_{v,i}\right) = (1/RT)\int_V^\infty\left[\left(\frac{\partial P}{\partial n_i}\right)_{T,V,n_j} - \frac{RT}{V}\right]dV - ln(Z) \tag{31}$$

In all of the above equations, *nc,* y_i, $h_{V,i}(T)$ and Z denote the number of components in the mixture, the molar fractions of the mixture components, the pure species vapor enthalpies and compressibility factor, respectively. A similar set of equations was applied to calculate the same parameters of the liquid phase.

2.8.8. Reactions and Component Concentrations

A set of non-linear equations was solved numerically for every reacting component to calculate the outlet stream concentration. It was assumed that the inlet materials are instantaneously mixed with those already in the reactor. This may cause some deviation in the simulation compared with the experimental results. The mass balance for component A that enters the reacting process follows the below equation:

$$0 = FC_{in} - FC_{out} - V_w r_A \tag{32}$$

$$r_A = \sum_{j=1}^{q} r_{Aj} \tag{33}$$

$$r_{Aj} = \frac{\nu_{Aj}}{\nu_{kj}} r_{kj} \tag{34}$$

where, F, C_{in}, C_{out} denote the volumetric flowrate, inlet and outlet concentrations of component A in equation (32). r_A is the combined reaction rate of component A, which is calculated using equation (34). In this equation, r_{Aj} is the reaction rate of component A due to reaction j and q is the overall number of reactions. The reaction rate of component A in each reaction is calculated by considering the rate reference component (k) of the same reaction through equation (34). In this equation, ν_{Aj} and ν_{kj} are the stoichiometric coefficients of components A

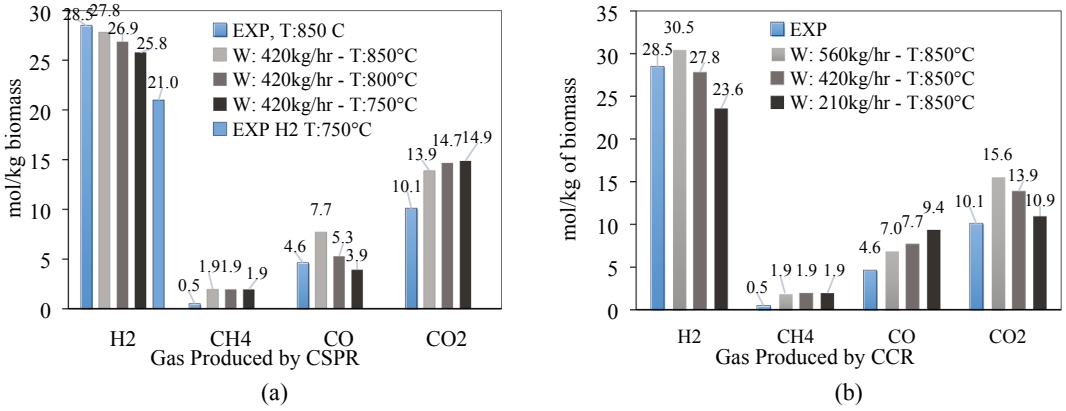

Fig. 8. Effect of water injection (W) and temperature (T) on hydrogen production in Solar Catalytic Steam Gasifier (SCSG).

and k. The general rate expression of reaction j is given by the below equation:

$$r_j = \frac{k\prod_{i=1}^{N} C_i^{\alpha_i}}{K_1 + C_m + C_n/K_2} \tag{35}$$

where C_i (kmol/m^3) and α_i are the concentration of component i and the order of the j-th reaction with respect to component i, respectively. If a component inhibits the reaction, it can be specified by the inhibition terms (Constants: K_1, K_2 and concentrations: C_m and C_n (kmol/m^3)). In this study, no inhibitory components were specified in the modeling process of the reacting systems. In addition, the reaction rate constant (k) for every kinetic reaction was calculated using the Arrhenius expression:

$$k_j = A_j exp\left(-\frac{E_j}{RT}\right) \tag{36}$$

where A_j and E_j are the pre-exponential factor and the activation energy of the j-th reaction.

For the stoichiometric reactions, calculation were done according to the molar stoichiometric coefficients (A_i) and the extent of reaction (x). The mass flow rates of the reference component (k) and any other component (i) were calculated using the below expressions:

$$F_{out,k} = F_{in,k}(1-x) \tag{37}$$

$$F_{out,i} = F_{in,i} - F_{in,k}x\left(\frac{A_i}{A_k}\right) \tag{38}$$

where, F_{out} and F_{in} denote the mass flowrate of the component after and before the reaction, and x and A refer the reaction extent and the component coefficient.

2.8.9. Absorption and Stripping

In this study, the thermodynamic model PSRK was implemented for modeling the CO_2 capture process with methanol and predicting the vapor pressure, liquid density, heat capacity, enthalpy, and phase equilibrium calculations. These calculations were conducted using PRO/II. Diffusivity and equilibrium conditions, according to Henry's law, were used in SuperPro Designer and the absorption specifications were adjusted as per PRO/II results. The binary interaction parameters of PSRK were revised by data from DECHEMA 2014 [38,39]. PSRK method is the best thermodynamic model for the analysis of the desorption tower and modeling the N_2 stripping tower. However, the analysis of SuperPro Designer is conducted through diffusivity constants and equilibrium functions.

$$P = \frac{RT}{V-b} - \frac{a(T)}{V(V+b)} \tag{39}$$

$$b = \sum_i x_i b_i \tag{40}$$

$$b_i = 0.08664R\frac{T_{ci}}{P_{ci}} \tag{41}$$

$$a(T) = \sum_i \sum_j x_i x_j (a_i a_j)^{1/2}(1-k_{ij}) \tag{42}$$

$$a_i = a_{Ci}\alpha_i \tag{43}$$

$$a_{Ci} = 0.42747(RT_{Ci})^2/P_{Ci} \tag{44}$$

$$\alpha^{0.5} = 1 + m_i\left(1 - T_{Ci}^{0.5}\right) \tag{45}$$

$$m_i = 0.480 + 1.574\omega_i - 0.176\omega_i^2 \tag{46}$$

where, T_{Ci}, P_{Ci}, ω_i, k_{ij}, denote the critical temperature, pressure and acentric factor of component i and k_{ij} is the binary interaction constant for components i and j, given by the following equation:

$$k_{ij} = a_{ij} + b_{ij}\frac{T_{ref}}{T} + c_{ij}ln\left(\frac{T_{ref}}{T}\right) \tag{47}$$

In SuperPro Designer, Henry's law was used for the simulation of absorption and stripping in Rectisol unit. Henry's law state that the solubility of a gas in a liquid us proportional to the partial pressure of the gas. It can be expressed in either solubility form (eq (48)) or volatility form (eq (49)).

$$X_2 = k_H P_2 \tag{48}$$

$$P_2 = K_H X_2 \tag{49}$$

where X_2 is the mole fraction of the dissolved gas and P_2 is the partial pressure of the gas above the liquid. K_H is the inverse if k_H. In this study, the latter form was used and the values of Henry's constants were extracted from [40].

3. Results and discussion

3.1. Model validation

The results of the techno-economic analysis greatly depend on the accuracy and reliability of the simulation. In this study, the simulation results of the dryer, screw conveyor, grinder, and cyclones have been compared with the commercial ones. The simulation results of the CSPR reactor (biomass refinery) are compared with the experimental results of the same process, done by our consortium at the University of Wyoming [6] and presented in Fig. 8. Additionally, the simulation results of the

Table 7
Validation of Rectisol process results produced by SuperPro Designer against those by PRO/II.

PRO/II				SuperPro Designer			
Name	**Flowrate (kg/h)**	**T (°C)**	**P(bar)**	**Name**	**Flowrate (kg/h)**	**T (°C)**	**P(bar)**
S1	MeOH: 7978	−55	32	S-114	MeOH: 8000	−55	32.3
S3	H_2: 262	−55	32	S-186	H_2: 260.6	−51.3	32.3
S2	MeOH:8000, CO_2: 1615	−26	32	S-116	MeOH:8000, CO_2:1615	−24.9	32.3
S4	MeOH:7980, CO_2: 1797	−40	32	S-228	MeOH:8000, CO_2:1615	−40	32.3
S4_2	MeOH:3990, CO_2: 898.6	−40	32	S-142	MeOH:4000, CO_2:807.7	−40	32.3
S5	MeOH:1.6, CO_2: 1797	–22.6	32	S-148	MeOH:3.6, CO_2: 1756	−37.3	32
S6	MeOH:3991, CO_2: 2128	−18.1	32	S-155	MeOH:4000, CO_2:1978	−10.3	32.3
S10	MeOH:0.047, CO_2: 85.66	−27.16	7.5	S-158	MeOH:3.6, CO_2: 36.99	−25.6*	7.5
S12	MeOH:3991, CO_2: 2042	−27.16	7.5	S-144	MeOH:3996, CO_2: 1941	−25.6*	7.5
S14	H_2:262.4, CO_2: 3027	–33.7	32	S-113	H_2:263.3, CO_2: 2926	–32.7	32
S15	MeOH:6467, CO_2: 2142	−37.48	4	S-165	MeOH:7069, CO_2: 2270	−31	4
S17	CO_2: 1559	−42.58	3	S-169	CO_2: 1358	−42	3
S18	MeOH:6467, CO_2: 1822	−42.33	3	S-166	MeOH:7069, CO_2: 2264	−45.9	3
S22	MeOH:019, CO_2: 916	−25	3	S-164	MeOH:14, CO_2: 1358	−25	3
S23	MeOH:8780, CO_2: 1426	−53	2	S-173	MeOH:9454, CO_2: 1741	−46.5	2
S24	N_2: 1960	25	2	S-170	N_2: 2000	25	2
S25	N_2:1960, CO_2: 1399	−60	2	S-171	N_2:2000, CO_2: 1247	−40.7	2
S26	MeOH:8779, CO_2: 27	−63	2	S-172	MeOH:9454, CO_2: 138	−49.6	2
S31	MeOH:7980, CO_2: 24.7	50	2	S-176	MeOH:7941, CO_2: 116.4	50	2
S37	MeOH:1233 CO_2: 29.6, H_2S:4.1	68	1.2	S-153	MeOH:1980, CO_2: 23.3, H_2S:3.5	68	2
S39	MeOH:1204, CO_2:4.8, H_2S:1.7	55	1.2	S-179	MeOH:1959, CO_2:0,H_2S:1.38	49.9	1.2
S33	MeOH:9557, CO_2:0, H_2S:0	68	1.2	S-183	MeOH:9901, CO_2: 116,H_2S:0.8	53.8	2
S35	MeOH:1602, CO_2: 0, H_2S:0	100	1.2	S-190	MeOH:1980,CO_2: 23.3,H_2S:0.16	100	1.2

Table 8a
Validation of ASU results produced by SuperPro Designer against those by PRO/II, 2700 kg/hr air.

PRO/II				SuperPro Designer			
Name	**Flowrate (kg/h)**	**T (°C)**	**P(bar)**	**Name**	**Flowrate (kg/h)**	**T (°C)**	**P(bar)**
S1	N_2: 2075, O_2:636	25	1.3	S-237	N_2: 2071, O_2:628.8	25	1.3
S2	N_2: 2075, O_2:636, efficiency:70%	260.5	6.2	S-126	N_2: 2071, O_2:628.8, efficiency:70%	259.7	6.2
S3	N_2: 2075, O_2:636	−173	6.2	S-125	N_2: 2071, O_2:628.8	−173	6.2
S4	N_2: 1572.4, O_2:636	−174.9	5.7	S-249	N_2: 1656.9, O_2:622.5	−181	5.7
S5	N_2: 503.14	−177.5	5.7	S-242	N_2: 414, O_2:6.3	−177	5.7
S6	N_2: 503.14	−185.5	1.3	S-241	N_2: 414, O_2:6.3	−177	1.3
S7	N_2: 503.14	−196	1.3	S-123	N_2: 414, O_2:6.3	−196	1.3
S8	N_2: 709.1, O_2:113.97	−191	1.3	S-243	N_2: 662.8, O_2:124.5	−185	1.3
S9	N_2: 863.3, O_2:522, CO_2:1.46	−191	1.3	S-248	N_2: 994.2, O_2:498	−185	1.3
S10	N_2: 2075.5, O_2: 0	−194	1.2	S-124	N_2: 2054, O_2:12.5	−195.8	1.2
S11	O_2: 636, N_2: 0	−181	1.2	S-120	O_2: 616.3, N_2: 16.56	−181	1.2

Table 8b
Validation of ASU results produced by Superpro Designer against those by PRO/II, 5000 kg/hr air.

PRO/II				Superpro Designer			
Name	**Flowrate (kg/h)**	**T (°C)**	**P(bar)**	**Name**	**Flowrate (kg/h)**	**T (°C)**	**P(bar)**
S1	N_2: 3819, O_2:1170	25	1.3	S-237	N_2: 3835, O_2:1164	25	1.3
S2	N_2: 3819, O_2:1170, efficiency:70%	260.5	6.2	S-126	N_2: 3835, O_2:1164efficiency:70%	259.7	6.2
S3	N_2: 3819, O_2:1170	−173	6.2	S-125	N_2: 3835, O_2:1164	−173	6.2
S4	N_2: 2893, O_2:1170	−174.9	5.7	S-249	N_2: 3068, O_2:1152	−181	5.7
S5	N_2: 925.99	−177.5	5.7	S-242	N_2: 767, O_2:11.6	−177	5.7
S6	N_2: 925.99	−185.5	1.3	S-241	N_2: 767, O_2:11.6	−177	1.3
S7	N_2: 925.99	−196	1.3	S-123	N_2: 767, O_2:11.6	−196	1.3
S8	N_2: 1305, O_2:209.7	−191	1.3	S-243	N_2: 1227.4, O_2:461	−185	1.3
S9	N_2: 1588.8, O_2:960, CO_2:2.69	−191	1.3	S-248	N_2: 1841.4, O_2:691	−185	1.3
S10	N_2: 3819.9, O_2: 0	−194	1.2	S-124	N_2: 3805, O_2:23	−195.8	1.2
S11	O_2: 1170.5, N_2: 0	−181	1.2	S-120	O_2: 1140.6, N_2: 30.7	−181	1.2

acid gas removal unit (Rectisol) and air separation unit by the SuperPro Designer are validated by thermodynamical simulation of these two processes using PRO/II at the steady-state condition. The simulation results including the mass flow rate, temperature, and pressure of the corresponding streams are summarized in Tables 7 and 8a,b (for two different flow rates). A separate thermodynamic modeling has also been conducted to investigate the catalyst regeneration unit using CO_2. This simulation was conducted by FactSage. The results have been depicted in Figure (13). Calculations related to the solar photovoltaic (PV) section has been conducted based on a comprehensive set of data collected from the available literature. A separate set of references for the solar PV section are provided in the supplementary information.

3.2. Biomass refinery unit

The results of H_2, CO_2, CO, and methane production as a function of

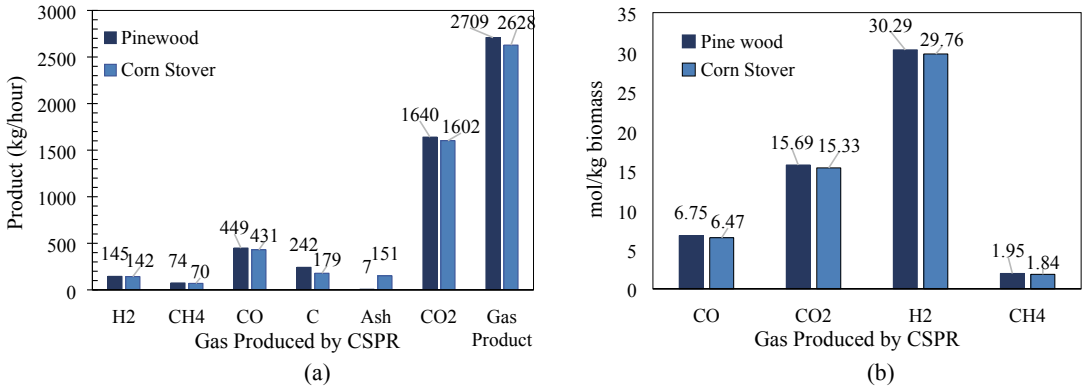

Fig. 9. The effect of biomass type on a) products of CSPR from corn stover and pine wood feedstocks and b) comparison of the syngas produced using corn stover and pine wood feedstocks.

temperature (750–850 °C) and water injection rate have been summarized in Fig. 8a and 8b, respectively. As observed, the production of hydrogen and carbon monoxide increased with temperature. However, the production of CO_2 decreased with temperature. In particular, the simulated results for H_2 production using 420 kg/hr water injection rate at 850 °C is in very close agreement with the experimental results. However, the simulated CO_2 production is higher than observed in experimental results. This could be due to the impact of COC catalyst in experiments and the lack of kinetic information in the simulation of the catalyst impact.

A significant impact was observed when water injection rate was varied at 850 °C. The total gas production reached the values of 45.7, 51.3, and 54.8 mol/kg biomass by increasing the water injection rate from 210 to 420 and 560 kg/hr per 3000 kg/hr of wet biomass (equivalent to 2350 kg/hr dried biomass) at 850 °C. Increasing the water injection rate led to a higher H_2/CO molar ratio under the same temperature. In contrast, the CO/CO_2 ratio decreased with increasing water injection rates. The increasing of H_2/CO and decreasing of CO/CO_2 with water injection rates have also been reported in the experimental results [6]. It is also observed that the H_2/CO molar ratios decreased with temperature at a constant water injection rate, also found in experimental results. All these agreements between the experimental and the TEA simulation results of the CSPR reactor demonstrate the validity of using the TEA results for the modeling of the SCCLBR power plant.

Although TEA simulation in this study was conducted based on the lignocellulosic structure of pinewood to be aligned with the experiments, corn stover is the ultimate feedstock target. The United States produces over 345 million metric tons of corn per year (as of 2019/2020), and is the largest producer of corn in the world [41]. According to the literature, the lignocellulosic content of corn stover is very similar to that of pine wood (Table 1): pine wood and corn stover are made of almost 34.28 and 33.75 cellulose and 19.78 and 22.08 hemicellulose, respectively (normalized with 24% moisture content). However, corn stover contains slightly lower lignin and a higher amount of ash which can affect the amount of tar produced. On the other hand, most of the tar produced in the CSPR reactor is converted to syngas in a tar reformer reactor. This conversation is also supported by the simulation results provided in Fig. 9a and b. As observed, a slightly lower amount of syngas is projected to be produced by assuming corn stover as the feedstock. In contrast, ash production has significantly been increased.

3.2.1. Rectisol unit

The lack of thermodynamic models and sufficient literature data about the diffusivity constant were the major challenges of the Rectisol simulation using SuperPro Designer. Yet, the comparison of the corresponding streams entering or leaving the absorbers, strippers, and flash drums demonstrated that all the TEA simulation data reasonably match the thermodynamic simulation in terms of flow rate, temperature, and pressure. Particularly, a perfect match is observed between the pressures of the corresponding streams. The temperature in Rectisol process varies between + 100 to −55 °C. Therefore, up to 5–6 °C difference can be considered a reasonable agreement between the temperatures modeled by the two simulation packages. However, major differences (above 10 °C mismatch) were observed in the three streams of S-148, S-171, and S-183 with their corresponding streams modeled using PRO/II. S-171 has caused some deviation between the CO_2 adsorption results between PRO/II and SuperPro Designer. This deviation is due to the larger flow rate of S-173, which is consequently due to the lower absorption of P-39 compared with the corresponding column in PRO/II (H_2S concentrator). Rectisol process is complex, with at least 5 interwoven loops. Any minor deviation in analysis can be boosted in different loops, ending up with a bigger deviation in the final results. Overall, simulation using thermodynamic equations using Pro/II showed a higher CO_2 removal compared to technical simulation using diffusion equation. However, to be more conservative in the final economic analysis of the SCCLBR plant, the lower CO_2 absorption was considered as the base of TEA analysis.

3.2.2. Air separation unit

A simplified flowsheet of the ASU modeled by PRO/II is shown in Fig. 7. This configuration was simulated at a high pressure (HP) column, including 45 trays (stages) operating at a pressure of 5.7 bar and a corresponding low pressure (LP) column including 70 trays (stages) operating at a pressure of 1.2 atm. The flowsheet was solved using the SRK with the following binary interaction parameter: $N_2/O_2 = -0.0133$. This cryogenic air separation process is started by compressing, cooling, and partially liquifying the air at the inlet of the unit. A part of the nitrogen is separated in the first column, while the rest of the nitrogen and oxygen are condensed. The liquid bottom product of the high-pressure column, which is rich in oxygen is flashed under an isothermal condition. The gaseous and liquid product streams are both injected to the middle of the LP column, where it is further cooled to separate oxygen and nitrogen from each other through the Joule-Thomson (JT) effect [42]. Table 8a shows the final specifications of each stream. As observed, oxygen (purity of 97.8%) and nitrogen (purity of 99.3%) were obtained by TEA simulation which is in a perfect match with the corresponding results obtained by PRO/II. In terms of energy recovery, the air separation unit also consists of a multi-step heat exchanger against the inlet airflow that recovers refrigeration from the product streams and cools the incoming flow, and hence the products leave the unit at near ambient temperatures. The refrigeration recovery saves (recycles) 30% of the consumed energy.

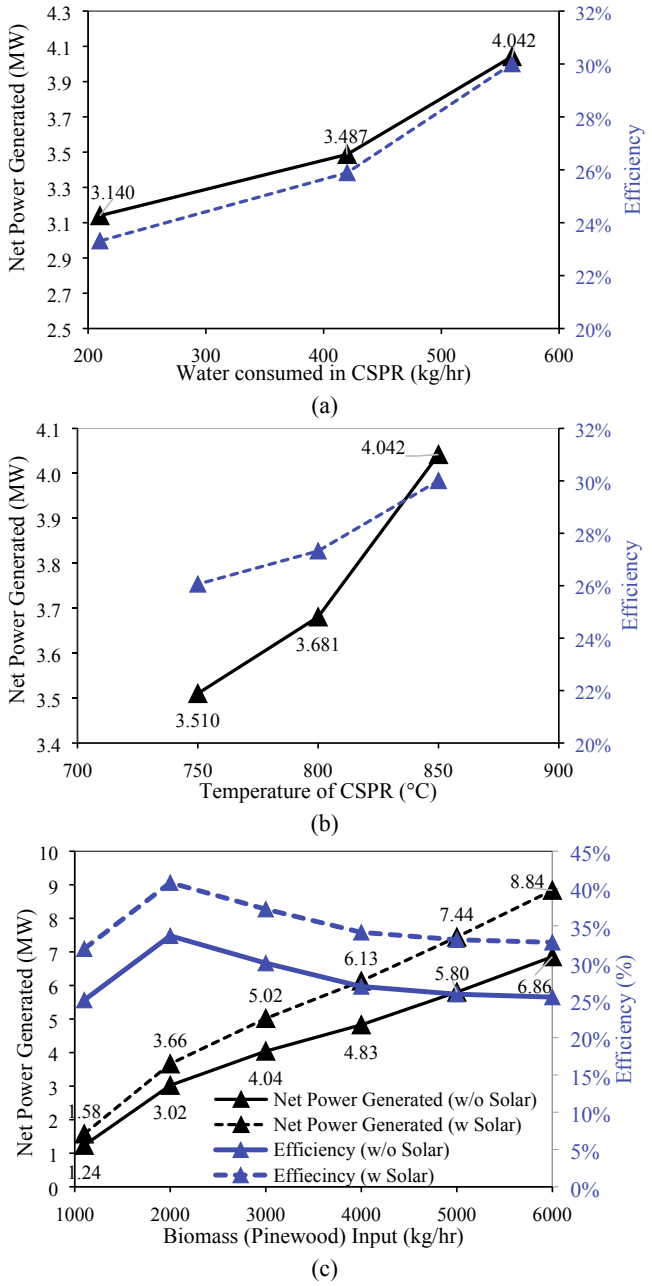

Fig. 10. CSPR power generation and efficiency at varying a) water injection rates, b) temperature, and c) feedstock inputs. Fig. 10c also illustrates the impact of deriving 50% of the CSPR power requirement from solar input. Dash Line: efficiency, Solid Line: Power generation.

3.3. Power generation and energy efficiency

The amount of power generated and the energy efficiency are the most important characteristics of every power plant. The energy efficiency is defined as the ratio of energy produced to the summation of the energy consumed:

$$\lambda = \frac{E_{out}}{E_{in}} \times 100\% \tag{50}$$

where λ, E_{out} and E_{in} denote the energy efficiency, the product energy output (MW) and the total energy consumption, including the summation of the energy of raw material, electricity, and steam (MW).

Fig. 10 describes the effects of CSPR temperature, water injection, and biomass loading on net power generation (MW) and water consumption per hour. Increasing the CSPR temperature from 750 to 850 °C increased the power generation and energy efficiency by 0.53 MW and 3.9% respectively. The same values will improve by 0.9 MW and 6.7% by increasing the water injection rate from 210 to 560 kg/hr at 850 °C. Accordingly, the maximum water injection rate and CSPR temperature were considered for analyzing the impact of biomass loading rate. The TEA simulation results also demonstrate that a SCCLBR plant on a scale of 1 to 6 tonne/day yields a hydrogen production equivalent to 1.24 to 6.86 MW. The power plants based on gasification technology with gas engine/steam turbine with scale $\geq$ 5MWe can offer the net electricity efficiencies of about 28%, which is comparable to that of coal-fired plants. However, the SCCLBR can reach an efficiency of 34% (using the most conservative S/B ratio and minimum energy recovery in different units). As observed the highest energy efficiency (not optimized) with an S/B ratio of 0.236 can be obtained at a federate of 2000 kg of biomass/hr. The efficiency is lower for higher biomass loading due to the insufficient steam injection. Yet, this value is only the baseline of the project. The process has the potential to reach a higher efficiency with the optimization of different units.

3.4. Hybridization with solar PV

Solar PV and concentrating solar power (CSP) systems are the two methods used for harnessing solar energy. PV systems directly convert solar radiation into electricity through the photovoltaic effect. The principle of PV solar cells is based on the release of electrons of semiconductors after absorption of photons. Single- or multi-crystalline-silicon and thin-films are among the commonly used non-organic material-based PVs. The CSP systems concentrate and accumulate the solar thermal energy to a receiver that serves as a heat source. An intermediate medium (the heat transfer fluid) is then used for the transfer of thermal energy, which is ultimately used to drive a turbine and subsequently produce electrical power [43]. Parabolic trough, central receiver, paraboloidal dish, solar chimney, and solar pond are the different categories of CSP systems. At a minimum, three scenarios can be considered for the integrated solar catalytic biomass refinery (SCCLBR) unit in this study. In the first scenario, the molten salt mixture can be used as the heat transfer fluid to store and transport solar thermal energy between the solar receiver and the biomass refiner. For this configuration, a solar energy collection unit can be employed to heat a solid mixture of $NaNO_3$ and KNO_3. The high-temperature molten salt liquid is then transferred to the shell side of the CSPR to provide the necessary heat for the steam pyrolysis of biomass. However, the commonly used molten salts, such as solar salt (60 wt%$NaNO_3$ + 40 wt% KNO_3) operate between 290 and 550 °C. Moreover, a high melting point (220 °C) and poor thermal stability limit their applications [44]. Hence, a multi-stage CSPR would be necessary for efficiently enhancing gas and solid conversions and sufficient utilization of biomass-derived syngas. It has also been reported that a multistage reaction can increase the total residence time, resulting in higher char conversion and releasing more energy from the fuel [45]. In the second scenario, concentrated solar energy as the high-temperature heat source can be used by the CSPR reactor directly to produce syngas while enabling solar energy storage into dispatchable fuels [46,47]. However, a significant technology development effort is still needed to ensure the temperature homogeneity, feasibility, and reliability of the solar reactor during the continuous process. Thermal simulation of the solar reactor is an essential part of such a TEA analysis. The third scenario, and the one considered for this study, uses a hybrid solution that integrates the PV solar cells with the CSPR reactor. The hybridization of various renewable energy sources can allow for smooth, stable, and reliable operation. The optimization of such a process offers the opportunity to tackle limitations on fuel availability, emissions, and economics. According to the simulation results in terms of energy production, hybridization of the CCLBR with solar PV to supply 50% of the energy required by the CSPR reactor can

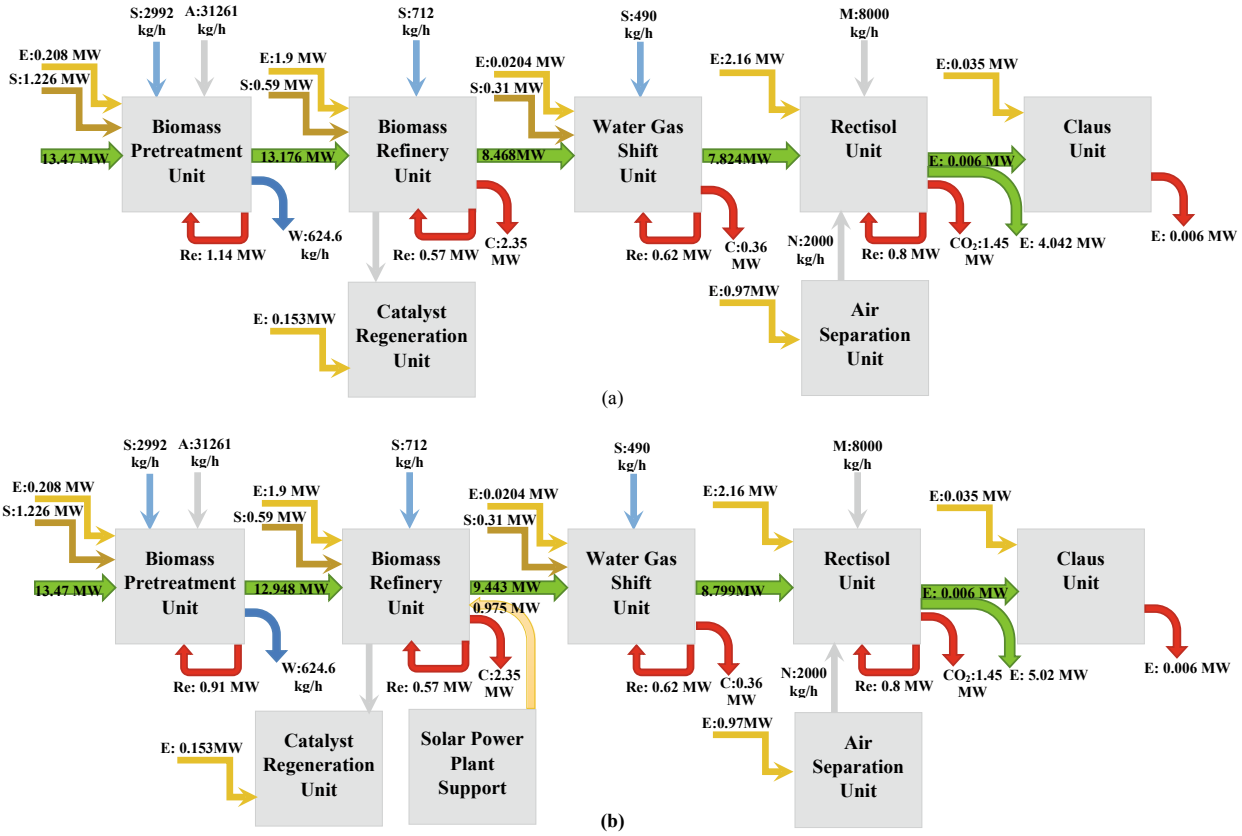

Fig. 11. Exergy flowchart of the a) catalytic chemical looping biomass refinery and b) solar catalytic chemical looping biomass refinery (SCCLBR) power plant. E: Electricity, S: Steam, A: Air, N: Nitrogen, M: Methanol, C: Carbon (Char), Re: Recoverable. **Note:** Pinewood biomass: 3000 kg/hr, T = 850 °C, Water = 560 kg/hr.

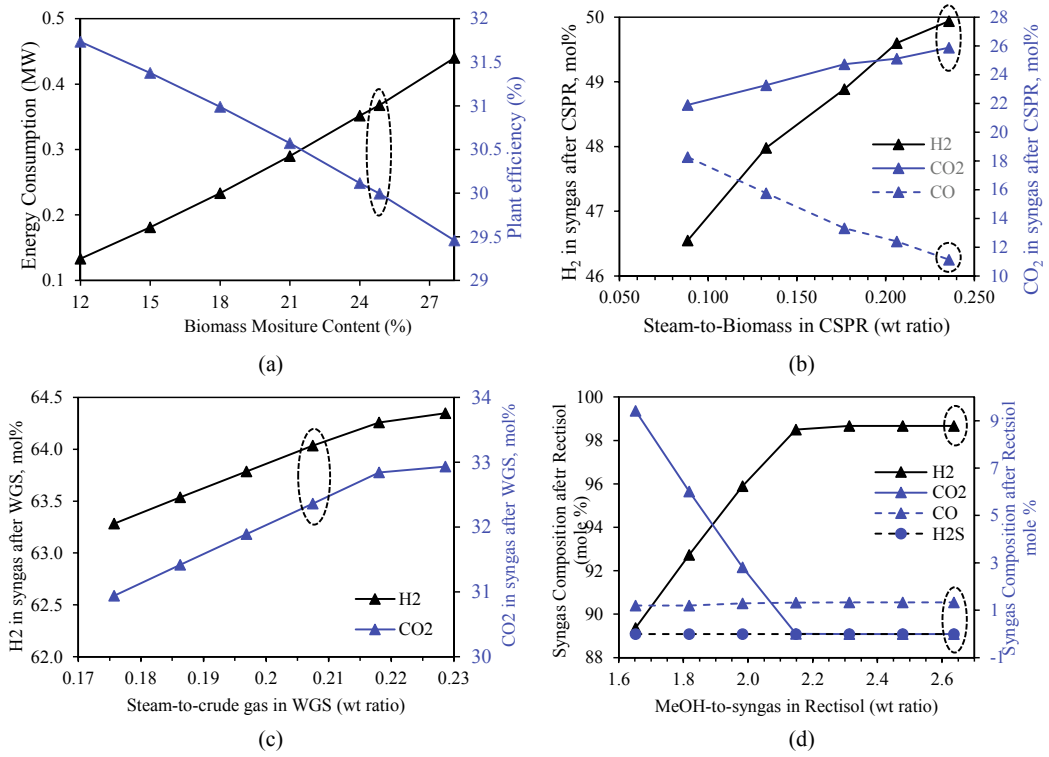

Fig. 12. a) Effect of biomass moisture on energy consumption by rotary dryer and its impact on plant efficiency, effect of b) water consumed in CSPR, c) water consumed in WGS unit, and d) methanol flow rate in Rectisol on syngas composition. Note: circled points represent the operating parameters used for the simulation of the plant.

further increase the efficiency of the plant to 40.8% (Fig. 11b). As observed in Fig. 10c, the power production in a small-scale (1 tonne/hr) SCCLBR plant increase from 1.24 to 1.58, while the power production has the potential to reach 8.84 MW on a larger scale (6 tonnes/hr) compared with CCLBR. However, the capital cost of the plant needs to be optimized against the power efficiency.

3.5. Exergy analysis

The exergy flowchart of pinewood conversion to hydrogen using the catalytic chemical looping biomass refinery (CCLBR and SCCLBR) power plant (without and with solar energy support) is demonstrated in Fig. 11. The CSPR operating conditions are 850 °C with a water injection rate of 0.236 steam/biomass (dry weight basis). The biomass refinery, Rectisol process, and ASU account for the highest energy consumption units of the plant accounting for 48.9%, 38%, and 17% of energy consumption, respectively. The total energy loss of the plant due to the carbon loss in the biomass refinery unit and CO_2 removal in the Rectisol unit accounts for 3.15 MW, equivalent to 23.4% of the energy input. In addition to non-recoverable energy losses, a portion of energy in the outlet streams of biomass pretreatment and biomass refinery can be recovered by producing high-temperature steam and/or heating the inlet stream. In terms of the Rectisol unit, the cooling energy is recovered to reduce the temperature of methanol. In conclusion, At a feed rate of 3000 kg/hr of pinewood biomass, 42% of the lower heating value of the feedstock is consumed in the SCCLBR power plant, and 23.4% is lost. To further enhance the exergy efficiency of the biomass to hydrogen process, a solar biomass refinery is proposed. A biomass refinery under the above-mentioned operating conditions consumes 1.9 MW of energy, 50% of which can be supplied by solar energy. This can further reduce the energy consumption by 0.975 MW, which increases the energy efficiency of the plant by up to 7.3% (details of the process is observed in Fig. 11b).

3.6. Key parameter analysis

The total hydrogen produced and the overall efficiency of the SCCLBR power plant closely depend on the performance of each unit and the proper selection of key adjustable parameters: biomass moisture content in the pretreatment unit, steam-to-biomass ratio in the refinery unit, steam-to-crude gas in the WGS unit, and methanol flow rate in the Rectisol unit. The results have been summarized in Fig. 12. Catalyst regeneration is an important factor in chemical looping process. In the catalyst regeneration unit, pressure and temperature play key roles, which will be discussed separately in the next section. In the air separation unit (ASU), although operating conditions and design of the distillation columns play an important role, the gas flow rate (unit capacity) is the key. Given that the Rectisol unit uses nitrogen, the capacity of the ASU is related to the Rectisol process. The Claus process has not been studied in terms of the key parameter analysis since the simulation in this unit is partially based on the stoichiometry of the reaction rather than the kinetics.

3.6.1. Pre-treatment unit

The initial moisture content of the biomass plays a key role in power consumption by the biomass pretreatment unit. As observed in Fig. 12a, the rotary dryer has a power requirement of 0.133 MW/hr for removing the moisture (from 12% to 5.1%), considering 70% of energy recovery from the outlet hot steam and 70% energy efficiency of the dryer. However, the power consumption increases by more than 3 times for drying biomass with 28% moisture content. This subsequently reduces the plant efficiency by 2.3%. Any reduction in heat recovery may cause a higher reduction in plant efficiency. In this study, the initial and final moisture contents of 24.85% and 5.1% were considered for the simulation of the SCCLBR. A higher final moisture content (at the inlet of the CSPR) has a negative impact on the energy consumption in the biomass refinery unit and a larger amount of heat has to be consumed by the CSPR to evaporate water at a lower temperature [48]. This highlights the impact of natural drying which is energetically free but can significantly affect the efficiency of the plant, although the seasonal and regional parameters must be considered as well.

3.6.2. Biomass refinery unit (SCPR reactor)

The effect of steam-to-biomass and temperature on hydrogen production per kg of biomass was discussed in the previous section. This section focuses on the relationship between the syngas composition and steam-to-biomass ratio (as the key parameter). The results have been presented as the ratio to the initial dried biomass (2375 kg/h, which is equivalent to 3000 kg/hr of wet biomass). Fig. 12b demonstrates that the mole fraction of hydrogen in syngas increases from 46.5 to 50% with increasing steam-to-biomass ratio from 0.088 to 0.236 (equivalent to 210 to 560 kg/hr steam injection). This increase is equivalent to almost 16 kmol/hr increase in hydrogen production, which can increase the plant efficiency by up to 7%. On the other hand, CO content decreases from 18 to 11%, while CO_2 increases from 22 to 26%. This could be attributed to the water gas shift reaction and its consequent impacts. However, given that the SuperPro Designer considers an instant and perfect mixing of any compound in inlet streams with those already in the reactor, a higher quantity of water is needed in real chemical looping power plants.

3.6.3. WGS unit

Steam to crude gas (dry basis) is the key parameter for the water gas shift unit. The impact of steam-to-crude gas ratio on syngas composition is observed in Fig. 12c. Overall, the WGS unit increases the molar fraction of hydrogen in syngas from around 50% to 64% (considering a steam-to-crude gas ratio of 0.21). This is equivalent to the 24 kmol/hr increase in hydrogen production, which contributes to 12% of the plant efficiency. The increase of steam-to-crude gas ratio from 0.175 to 0.218 (weight ratio) increases the hydrogen production by 1 kmol/hr which can further increase the plant efficiency by 0.5%. Meanwhile, it can reduce the CO from 3% mole fraction to around 1% (not shown in the graph) and increases the CO_2 content from 31 to 33%.

3.6.4. Rectisol and ASU units

Poor methanol (absorbent) flowrate is the key parameter for the Rectisol unit. The methanol flowrate is a trade-off between purification capability and energy consumption. Fig. 12d demonstrates the impact of methanol flowrate on CO_2, H_2S, and CO concentration of the syngas according to the Pro/II results. Generally, the Rectisol unit increases the hydrogen mole fraction of syngas from around 64.5% to 98%. According to the results, H_2S is fully removed in different MeOH flow rates. Increasing the methanol-to-syngas (weight ratio, produced by WGS unit) from 1.65 to 2.15 significantly purifies the syngas (from 89 to 98.5% H_2 fraction). Further increasing the methanol flow rate does not significantly affect the H_2 concentration in syngas. However, it does have an impact on the design of the Rectisol unit. For example, at the minimum methanol-to-syngas ratio of 1.65, 36.5 mol% of the CO_2 is removed by the desorption unit (P-39 which reabsorb H_2S and desorb CO_2), while 63% of the CO_2 remains to be removed by the stripping unit. While at the maximum MeOH flow rate, this balance changes to 53.6 to 46.4%. Greater CO_2 removal by the stripping unit may need multiple striping steps, in addition to a higher N_2 injection. In either case, the design of the Rectisol unit and every single absorber, desorber and stripper play a key role in energy consumption and CO_2 removal. In the current simulation, the nitrogen flow rate of 2000 kg/hr has been considered. Further reduction of nitrogen is possible according to the Pro/II results. For example reduction of the nitrogen flow rate to 1500 or 1250 kg/hr, may cause 1.52% and 2.2% increase in the plant efficiency, respectively. However, it may cause 87 and 106 kg/hr lower CO_2 removal by the stripper unit at MeOH-to-syngas of 2.31 and 2.64 (wt ratio) and 1250 kg/hr N_2. Optimizing and balancing the relation between Rectisol and ASU is needed for this step.

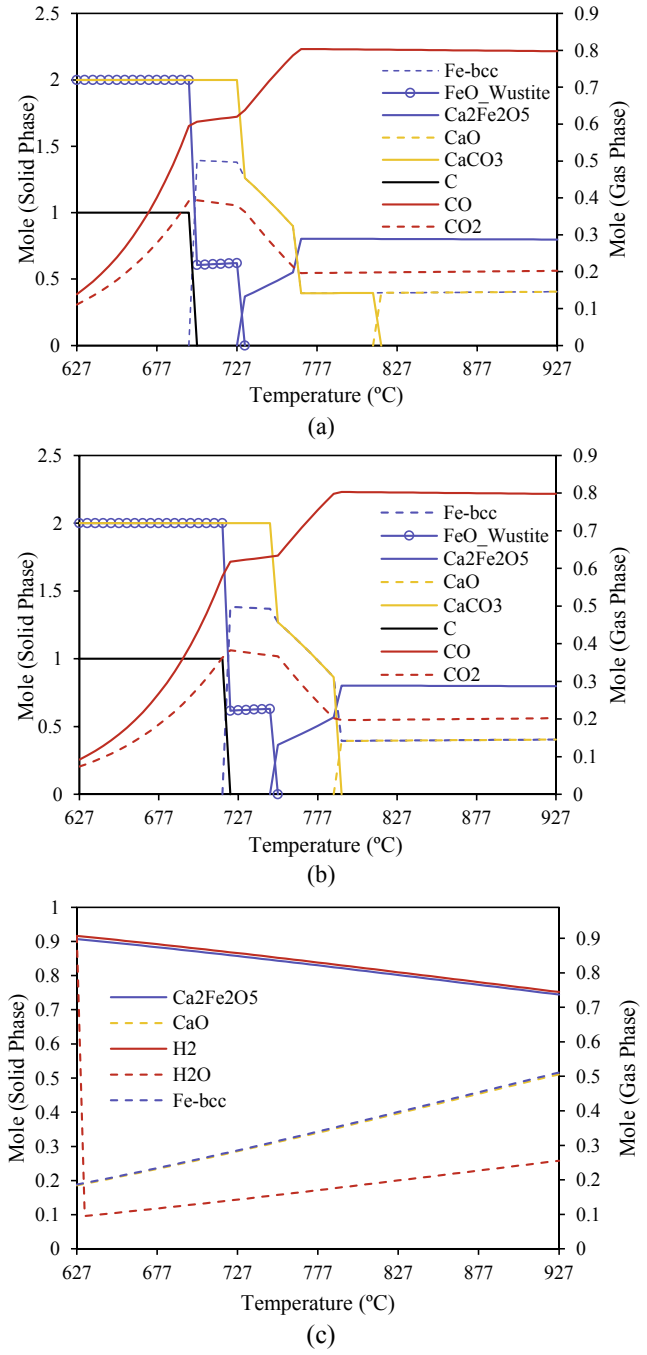

Fig. 13. The thermodynamic equilibrium of catalyst regeneration processes using a) CO_2 at 1 bar, b) CO_2 at 1.5 bar ($3CO_2 + 2Fe + 2CaO \rightarrow Ca_2Fe_2O_5 + 3CO$), c) steam at 1 bar ($3H_2O + 2Fe + 2CaO \rightarrow Ca_2Fe_2O_5 + H_2$).

3.6.5. Catalyst regeneration unit

This study proves the possibility of the regeneration of $Ca_2Fe_2O_5$ using CO_2 as the oxidizing agent through thermodynamic modeling. The results of the process under different temperatures (from 627 to 927 °C) and two different pressures (Fig. 13a:1bar and Fig. 13b:1.5 bar) have been summarized in Fig. 13. As observed, oxidizing the CaO and Fe is a temperature-dependent process and the final products vary by increasing the temperature. At temperatures below 700 °C, FeO and $CaCO_3$ are the main products. $CaCO_3$ remains one of the main products of the process at higher temperatures up to 727 °C. Meanwhile, FeO production gradually reduces and is replaced by the body-centered cubic pattern Fe (Fe-bcc). Regeneration of $Ca_2Fe_2O_5$ initiates at a temperature above 727 °C and is maximized at around 760 °C. At this temperature and above, CO_2 in the gaseous phase is mainly replaced by CO. Additionally, the transition of the Fe from BCC to FCC occurs at 900 °C, resulting in an 8 to 9% increase in density. Essentially the same pattern is observed at the CO_2 atmosphere of 1.5 bar. However, the process of $Ca_2Fe_2O_5$ regeneration is postponed by 20 °C and is maximized at 787 °C. These results are well aligned with the experimental observations. Thus, carbonation is avoided by operating at temperatures above the equilibrium temperature for pure CaO. A temperature higher than 730–750 °C during the oxidation of the reduced catalyst (CaO and Fe) is required to regenerate the $Ca_2Fe_2O_5$, while avoiding carbonation (Fe_2O_3 and $CaCO_3$ production). The other factor, which must be considered, is the impact of calcium. Without the presence of Ca, the reduced OC (Fe^0) could only be oxidized by CO_2 to generate Fe_3O_4 (1.33 mol CO/mol Fe)($3Fe + 4CO_2 \rightarrow Fe_3O_4 + 4CO$). Whereas, the process yields $Ca_2Fe_2O_5$ using the same moles of Fe oxidized by CO_2 and 1.5 mol CO/mol Fe. Fig. 13c represents the phase equilibrium of the $Ca_2Fe_2O_5$ using steam. As observed, no other side product is generated other than $Ca_2Fe_2O_5$ under temperature between 627 and 927 °C, proving that steam can regenerate this catalyst as well. This is expected to partially occur in the CSPR.

3.6.6. Biomass loading to the SCCLBR plant

Fig. 14 depicts the impact of feedstock loading on the gas composition and total hydrogen produced by the CSPR reactor (Fig. 14a) and SCCLBR plant (Fig. 14b). The simulation was conducted under the CSPR temperature of 850 °C and the same steam-to-biomass (S/B) ratio. The total hydrogen production in both the CSPR reactor and the SCCLBR plant increased linearly with feedstock loading. However, the concentration of hydrogen and CO_2 gradually decreased. Meanwhile, the quantities of CO and CH_4 have increased. This behavior was also observed in Fig. 8a (the impact of water), although the trend of reduction is lower in Fig. 14b. Accordingly, the most important potential reason could be related to the quantity of water as the gasifying agent. Further increase in water injection rate can potentially increase hydrogen production. However, the efficiency results clearly shows that the S/B ratio of 0.235 works the best for the biomass loading of 2000 tonne/hr. A multi-variable optimization of the process is needed to maximize the efficiency of the process under a larger biomass loading rate.

3.7. Greenhouse gas emissions

Greenhouse gas emissions are an important factor in investigating the performance of power plants. Reducing carbon dioxide (CO_2) as the primary greenhouse gas plays a key role in achieving carbon and climate commitments. In this study, the GHG factor is defined as the ratio of the total mass of CO_2 produced per ton of H_2:

$$GHG_{emission} = \frac{m_{CO_2}}{m_{H_2}} \tag{51}$$

where m_{CO2} and m_{H2} represent the amount of CO_2 and H_2 produced in the SCCLBR. The results of GHG emission under different CSPR operating conditions are summarized in Fig. 15. For pine wood feedstock, the GHG factor decreased from 10.54 to 10.4 as the CSPR temperature decreased from 850 to 750 °C, which is equivalent to 1694 tons of CO_2 reduction/year. A more significant CO_2 reduction is obtained by reducing the water injection to the CSPR from 560 to 210 kg/hr while a constant amount of water is used in WGS reactors (370 and 120 kg/hr in high and low-temperature WGS reactors) respectively. However, CO_2 reduction by both adjusting temperature and water supply of the CSPR comes at the cost of a significant reduction in power generation. In the second scenario, reduction of injection to CSPR (from 560 to 210 kg/hr) and increase of water used by H-WGS and L-WGS reactor caused a simultaneous increase of CO_2 emission and reduction of power

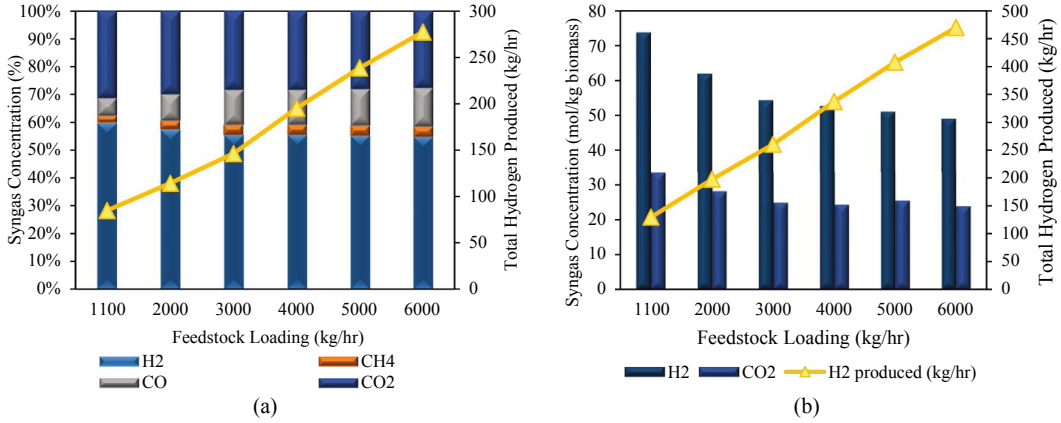

Fig. 14. The effect of feedstock loading on the gas composition and total hydrogen produced from a) the CSPR reactor and b) the SCCLBR power plant.

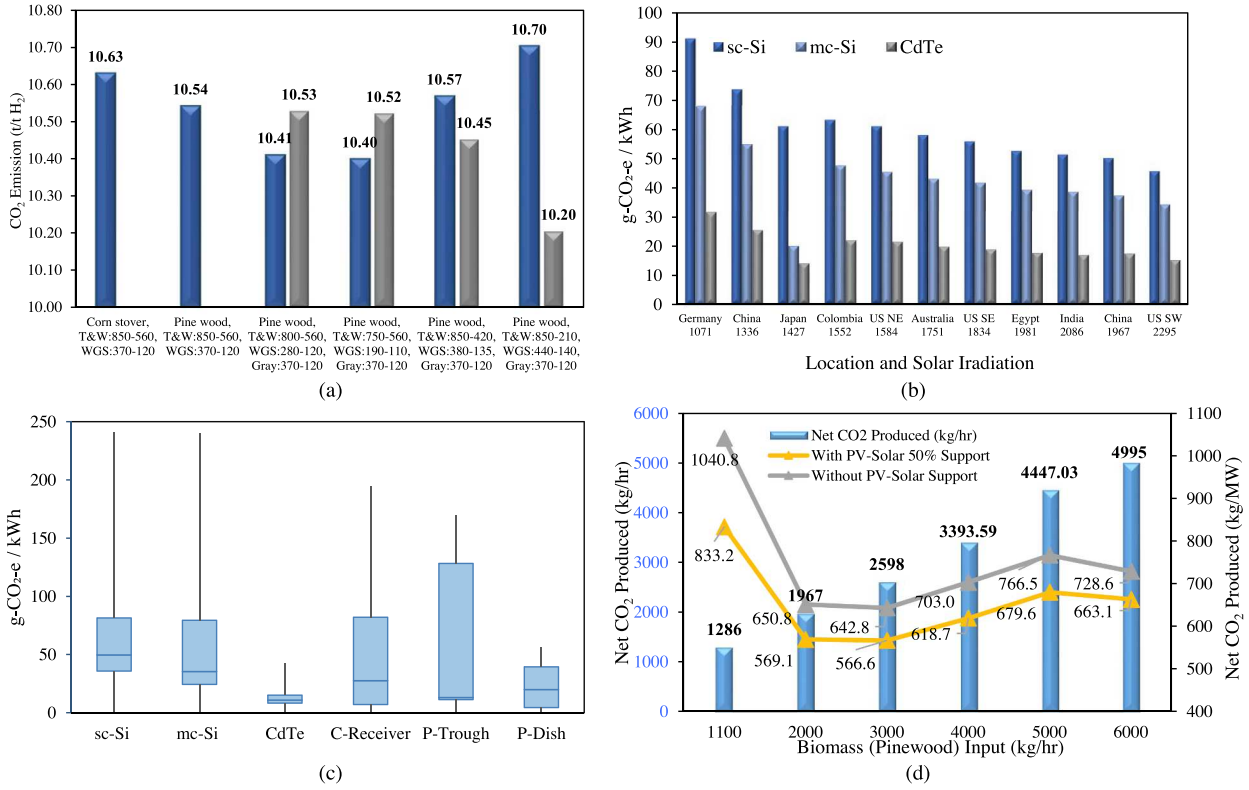

Fig. 15. a) Greenhouse gas emissions from the SCCLBR power plant per ton of H_2 produced, b) net CO_2 production from different PV cells/kwh of energy produced. c) Quadratile analysis based on the life cycle GHG emissions for solar electricity generation technologies, d) net CO_2 production from the SCCLBR at varying feedstock input rates, with and without 50% solar PV support.

generation. The GHG emissions under different biomass loading also have the average value of 10.25 CO_2/H_2 (weight basis). The maximum GHG emission in SCCLBR is 10.70 which is significantly lower than traditional coal-to-hydrogen (15.23) and biomass-to-hydrogen power plants (16.39).

Published results from 96 estimates of PV systems including crystalline silicon (c-Si) (mono-crystalline and multi-crystalline) and thin film (TF) (cadmium telluride [CdTe]) and CSP systems including Parabolic trough, central receiver, paraboloidal dish were reviewed and included in this study. The references have been separately cited in the supplementary information. The life cycle GHG emissions for solar electricity generation technologies are summarized in Fig. 15b and 12c. The results are well-matched with the life cycle greenhouse gas emissions from solar photovoltaics published by NREL, which are based on the results collected from 400 studies [49,50]. As observed, life cycle greenhouse gas (GHG) emissions from sc-Si solar cells with 50 g CO_2/kWh represented the highest net CO_2 production compared with the other solar energy. In the LCA literature on PV technologies, the assumed solar irradiation ranged from 900 to 2,300 kWh/m^2/yr. The quadratile values in Fig. 15c are very close to the GHG emissions for c-Si PV technologies with solar irradiation of 1,700 kWh/m^2/yr, typical for southern Europe. Establishing the plant in locations with higher solar irradiation and using a higher irradiation estimate (i.e., 2,300–2,400 kWh/m^2/yr, typical for the Southwestern U.S.) would result in proportionally lower GHG emissions (Fig. 15b). Fig. 15d shows the overall performance of the modeled SCCLBR in terms of GHG emissions based on six different loadings of feedstock. As observed, the CO_2 production increased from 1286 to 4995 kg/hr by changing the feedstock loading

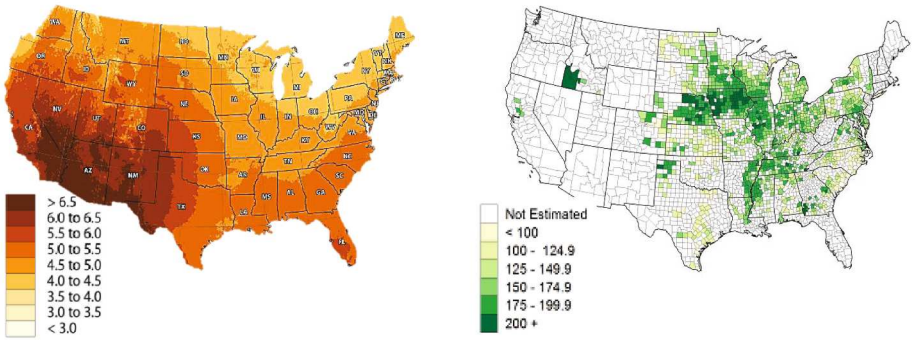

(a) (b)

Fig. 16. a) Photovoltaic Solar resources of the United States, Resource: National Renewable Energy laboratory, Unit: kWh/m^2/Day b) Corn for grain 2019 production by county, Unit: Bushies per acre, Resource: US Department of Agriculture.

from 1 to 6 tonne/hr. However, two points must be considered: 1) the rate of increasing the CO_2 emission reduced statistically and quantitatively from 52.9% (2 vs 1 tonne/hr) to 12.3% (6 vs 5 tonnes/hr), which is equivalent to 681 versus 547 kg/hr; 2) the estimated GHG emission per kW of electricity generated reduced from 1040 to 650–728 kg CO_2/kw by increasing the feedstock loading. Hybridization of the plant to supply 50% of the energy consumed by the CSPR reactor from PV solar cells can further reduce the CO_2 emission to as low as 566 kg CO_2/kw. Across varying feedstock input rates, greenhouse gas emissions average 12.8% lower when solar PV supplements refinery power needs. The maximum emission reduction by up to 19.9% was observed for the feedstock loading of 1 tonne/hr which is attributed to the greater steam/dry biomass ratio (0.64).

3.8. Simple Payback Time

It can be concluded from the results of the different analyses that the profitability of the SCCLBR production routes is highly dependent on the operating conditions of the CSPR reactor as well as the integration of the process with solar PV. Accordingly, the location of the plant in terms of accessibility to the biomass resources and high index of solar irradiation is the other key parameter. Fig. 16a and b demonstrates the locations with the maximum solar index as well as accessibility to the raw biomass (corn stover as the feedstock). More details about these figures can be found in the supplementary information (Figs. S1 and S2). A simple payback time (SPBT) was conducted to investigate the feasibility of integration of PV systems with CCLBR through the below equation:

$$SPBT = \frac{C_{cap}}{AEP^{*}P - C_{cap}{}^{*}i - C_{main}} \quad (52)$$

where, C_{cap}, AEP, P, i, and C_{main} denote the initial capital expenditure, annual energy production through PV system, energy price, interest rate and annual operation, and maintenance expenses (O&M). We considered the capital cost of 1.83 USD per Watt, O&M of 18 USD/kW-yr, and debt interest rate of 4.8% according to the most recent PV commercial modelling by the U.S. national renewable energy laboratory (NREL) [51] and U.S. Energy Information Administration (EIA) [52]. The SPBT provides insight into how long the solar PV system must work before the integrated SCCLBR plant can be considered a preferable alternative to the CCLBR counterpart. The results demonstrated the SPBT of 3.35 years for the establishment of the SCCLBR power plant in the western areas of the U.S. The SPBT can further be reduced to 3.06 years in the southwestern United States, which receives the greatest amount of solar energy. However, the SPBT increases up to 3.54 years in the southeastern United States, which receives a lower amount of solar energy. However, as observed the accessibility to the biomass resources is lower in locations with greater solar irradiation. Optimization of the plant location is required to balance the feedstock transportation cost and solar accessibility.

4. Conclusion

To evaluate the techno-economic feasibility of hydrogen production through a solar catalytic chemical looping biomass refinery (SCCLBR), a detailed parametric and economic analysis was conducted. The TEA combines process modeling and engineering design with economic evaluation. The results revealed that the CCLBR and SCCLBR power plant could reach an energy efficiency of 34%, which is 6% higher than the common gasification plants. The biomass refinery unit accounts for 21% of the total energy consumption in the plant. The SCCLBR can reach an efficiency of 34% (using the most conservative S/B ratio and minimum energy recovery in different units). According to the simulation results in terms of energy production, hybridization of the CCLBR with solar PV to supply 50% of the energy required by the CSPR reactor can further increase the efficiency of the plant to 40.8%. In addition, the thermodynamic analysis of the oxygen carrier catalyst ($Ca_2Fe_2O_5$), demonstrated the successful regeneration of its reduced form (CaO and Fe^0) using CO_2 at temperatures above 730 °C. It was also found that the maximum GHG emission in SCCLBR is 10.70 tons CO_2/ton H_2 produced, which is significantly lower than traditional coal or biomass-to hydrogen power plants. Optimization of operating conditions, the performance of different units, the ratio between the scale of CSPR to solar PV can further increase the efficiency of the plant. More importantly, the design of an integrated SCCLBR and solar power plant still needs much effort. The ratio of the SCCLBR scale to the solar side of the plant needs to be further optimized by considering the energy efficiency vs the capital investment of the plant. This study provided a baseline analysis of a SCCLBR power plant. Additional study is needed to understand the optimum design of the plant to offset the capital cost and maximize plant efficiency, increase energy production, and reduce GHG emissions. Future assessments should also consider the systems-level effects of integrating factors, including solar radiation and feedstock transportation variables in different seasons, to better understand the impacts on plant efficiency.

Declaration of Competing Interest

The authors declare that they have no known competing financial interests or personal relationships that could have appeared to influence the work reported in this paper.

Acknowledgment

The authors are grateful to the financial support of the National Science Foundation (NSF EPSCoR RII Grant No. OIA-1632899) of the United States.

Appendix A. Supplementary data

Supplementary data to this article can be found online at https://doi.org/10.1016/j.enconman.2021.114341.

References

[1] EIA. U.S. Energy Information Administration, Monthly Energy Review, Table 1.3 and 10.1, April 2020, preliminary data; 2020.
[2] T. Wang. Biomass energy - power plant capacity worldwide 2018; 2019.
[3] S. 2018. Biomass feedstock production availability - U.S. by resource 2016; 2016.
[4] Alipour Moghadam R, Yusup S, Azlina W, Nehzati S, Tavasoli A. Investigation on syngas production via biomass conversion through the integration of pyrolysis and air–steam gasification processes. Energy Convers Manage 2014;87:670–5.
[5] Im-orb K, Arpornwichanop A. Process and sustainability analyses of the integrated biomass pyrolysis, gasification, and methanol synthesis process for methanol production. Energy. 2020;193:116788.
[6] Sun Z, Chen S, Russell CK, Hu J, Rony AH, Tan G, et al. Improvement of H2-rich gas production with tar abatement from pine wood conversion over bi-functional Ca2Fe2O5 catalyst: Investigation of inner-looping redox reaction and promoting mechanisms. Appl Energy 2018;212:931–43.
[7] Im-orb K, Wiyaratn W, Arpornwichanop A. Technical and economic assessment of the pyrolysis and gasification integrated process for biomass conversion. Energy. 2018;153:592–603.
[8] Chai Y, Gao N, Wang M, Wu C. H2 production from co-pyrolysis/gasification of waste plastics and biomass under novel catalyst Ni-CaO-C. Chem Eng J 2020;382:122947.
[9] Dai B, Zhang L, Cui J-F, Hoadley A, Zhang L. Integration of pyrolysis and entrained-bed gasification for the production of chemicals from Victorian brown coal — Process simulation and exergy analysis. Fuel Process Technol 2017;155:21–31.
[10] Bartocci P, Zampilli M, Bidini G, Fantozzi F. Hydrogen-rich gas production through steam gasification of charcoal pellet. Appl Therm Eng 2018;132:817–23.
[11] Womac ARI, Sokhansanj C, Pordesimo S. BIOMASS MOISTURE RELATIONS OF AN AGRICULTURAL FIELD RESIDUE: CORN STOVER. Am Soc Agricult Eng 2005;48:2073–83.
[12] Shinners KJ, Binversie BN. Fractional yield and moisture of corn stover biomass produced in the Northern US Corn Belt. Biomass Bioenergy 2007;31:576–84.
[13] Database for the physico-chemical composition of (treated) lignocellulosic biomass, micro- and macroalgae, various feedstocks for biogas production and biochar; 2020.
[14] Pine Wood Pellet Production Line.
[15] WOODCHIP DRYERS.
[16] Haque N, Somerville M. Techno-Economic and Environmental Evaluation of Biomass Dryer. Procedia Eng 2013;56:650–5.
[17] C.B.s. Report. Drying solutions for Canadian biomass producers; 2017.
[18] C.M. Sales. HEIL 8X24 DRUM DRYER.
[19] Athanasiov A, Gupta ML, Fragar LJ. An insight into the grain auger injury problem in Queensland, Australia. J Agricult Safety Health 2006;12:29–42.
[20] Zareiforoush H, Komarizadeh MH, Alizadeh MR, Masoomi M. Screw conveyors power and throughput analysis during horizontal handling of paddy grains. The Journal of Agricultural Science. 2010;2:147–57.
[21] Dry Bulk Material Conveying.
[22] Spinelli R, Hartsough B. A survey of Italian chipping operations. Biomass Bioenergy 2001;21:433–44.
[23] Naimi LJ, Sokhansanj S, Mani S, Hoque M, Bi T, Womac AR, et al. Cost and Performance of Woody Biomass Size Reduction for Energy Production. St. Joseph, MI: ASABE; 2006.
[24] Liu G, Liao Y, Wu Y, Ma X. Evaluation of Sr-substituted Ca2Fe2O5 as oxygen carrier in microalgae chemical looping gasification. Fuel Process Technol 2019;191:93–103.
[25] Liu G, Liao Y, Wu Y, Ma X. Reactivity of Co-doped Ca2Fe2O5 brownmillerite oxides as oxygen carriers for microalgae chemical looping gasification. Int J Hydrogen Energy 2019;44:2546–59.
[26] Sikarwar VS, Zhao M, Clough P, Yao J, Zhong X, Memon MZ, et al. An overview of advances in biomass gasification. Energy Environ Sci 2016;9:2939–77.
[27] V. Marcantonio, A. Ferrario, A. Carlo, L.D. Zotto, D. Monarca, E. Bocci. Biomass Steam Gasification: A Comparison of Syngas Composition between a 1-D MATLAB Kinetic Model and a 0-D Aspen Plus Quasi-Equilibrium Model; 2020.
[28] Kumar A, Jones DD, Hanna AM. Thermochemical Biomass Gasification: A Review of the Current Status of the Technology. Energies. 2009;2.
[29] C3500 Steel Cyclone Separator, https://www.oneida-air.com/c-3500-galvanized-steel-cyclone-separator.
[30] CIPRES FILTER, AIR EXTRACTION AND FILTRATION, https://www.cipres.cz/en/produkt/cyclone-separators/.
[31] Elliott DC. Relation of Reaction Time and Temperature to Chemical Composition of Pyrolysis Oils. Pyrolysis Oils from Biomass. Am Chem Soc 1988:55–65.
[32] Guan G, Kaewpanha M, Hao X, Abudula A. Catalytic steam reforming of biomass tar: Prospects and challenges. Renew Sustain Energy Rev 2016;58:450–61.
[33] Abu El-Rub Z, Bramer EA, Brem G. Review of Catalysts for Tar Elimination in Biomass Gasification Processes. Ind Eng Chem Res 2004;43:6911–9.
[34] Zhu Q. High temperature syngas coolers. CCC/257. IEA Clean Coal Centre 2015.
[35] R. G., W. H. Separation of Gaseous Components From a Gaseous Mixture by Physical Scrubbing, . in: US Patent number 4, 567 (Ed.);1982.
[36] Gatti M, Martelli E, Marechal F, Consonni S. Review, modeling, Heat Integration, and improved schemes of Rectisol®-based processes for CO2 capture. Appl Therm Eng 2014;70:1123–40.
[37] Jones D, Bhattacharyya D, Turton R, Zitney SE. Rigorous Kinetic Modeling and Optimization Study of a Modified Claus Unit for an Integrated Gasification Combined Cycle (IGCC) Power Plant with CO2 Capture. Ind Eng Chem Res 2012;51:2362–75.
[38] Yang S, Qian Y, Yang S. Development of a Full CO2 Capture Process Based on the Rectisol Wash Technology. Ind Eng Chem Res 2016;55:6186–93.
[39] Yang S, Xiao Z, Deng C, Liu Z, Zhou H, Ren J, et al. Techno-economic analysis of coal-to-liquid processes with different gasifier alternatives. J Cleaner Prod 2020;253:120006.
[40] Jamali SH, Ramdin M, Becker TM, Torres-Knoop A, Dubbeldam D, Buijs W, et al. Solubility of sulfur compounds in commercial physical solvents and an ionic liquid from Monte Carlo simulations. Fluid Phase Equilib 2017;433:50–5.
[41] Statista. Global corn production in 2019/2020, by country. 2019-2020.
[42] Vinson DR. Air separation control technology. Comput Chem Eng 2006;30:1436–46.
[43] Kommalapati R, Kadiyala A, Shahriar MT, Huque Z. Review of the Life Cycle Greenhouse Gas Emissions from Different Photovoltaic and Concentrating Solar Power Electricity Generation Systems. Energies. 2017;10:350.
[44] Sun Z, Zeng L, Russell CK, Assabumrungrat S, Chen S, Duan L, et al. Solar–Wind–Bio Ecosystem for Biomass Cascade Utilization with Multigeneration of Formic Acid, Hydrogen, and Graphene. ACS Sustain Chem Eng 2019;7:2558–68.
[45] Meng WX, Banerjee S, Zhang X, Agarwal RK. Process simulation of multi-stage chemical-looping combustion using Aspen Plus. Energy 2015;90:1869–77.
[46] Bellouard Q, Rodat S, Grateau M, Abanades S. Solar Biomass Gasification Combined With Iron Oxide Reduction for Syngas Production and Green Iron Metallurgy. Front Energy Res 2020;8.
[47] Bellouard Q, Rodat S, Abanades S, Ravel S, Frayssines P-É. Design, simulation and experimental study of a directly-irradiated solar chemical reactor for hydrogen and syngas production from continuous solar-driven wood biomass gasification. Int J Hydrogen Energy 2019;44:19193–205.
[48] François J, Mauviel G, Feidt M, Rogaume C, Rogaume Y, Mirgaux O, et al. Modeling of a Biomass Gasification CHP Plant: Influence of Various Parameters on Energetic and Exergetic Efficiencies. Energy Fuels 2013;27:7398–412.
[49] NREL. Life Cycle Assessment Harmonization.
[50] NREL. Life Cycle Greenhouse Gas Emissions from Electricity Generation; 2013.
[51] Fu, R. Feldman, D. Margolis. R. U.S. Solar Photovoltaic System Cost Benchmark: Q1 2018. U.S. National Renewable Energy Laboraty (NREL)2018.
[52] Capital Cost and Performance Characteristic Estimates for Utility Scale Electric Power Generating Technologies. U.S. Energy Information Administration (eia); 2020.
[53] Qing Q, Zhou L, Guo Q, Gao X, Zhang Y, He Y, et al. Mild alkaline presoaking and organosolv pretreatment of corn stover and their impacts on corn stover composition, structure, and digestibility. Bioresour Technol 2017;233:284–90.
[54] Li, X. Dang, F. Zhang, Y. Zou, D. Yuan. H. Anaerobic Digestion Performance and Mechanism of Ammoniation Pretreatment of Corn Stover; 2015.
[55] Database for the physico-chemical composition of (treated) lignocellulosic biomass, micro- and macroalgae, various feedstocks for biogas production and biochar.
[56] Thoreson CP, Webster KE, Darr MJ, Kapler EJ. Investigation of Process Variables in the Densification of Corn Stover Briquettes. Energies 2014;7:1–14.
[57] Machado NT, de Castro DAR, Santos MC, Araújo ME, Lüder U, Herklotz L, et al. Process analysis of hydrothermal carbonization of corn Stover with subcritical H2O. J Supercri Fluids 2018;136:110–22.
[58] Mani S, Tabil LG, Sokhansanj S. Grinding performance and physical properties of wheat and barley straws, corn stover and switchgrass. Biomass Bioenergy 2004;27:339–52.
[59] Ranzi E, Cuoci A, Faravelli T, Frassoldati A, Migliavacca G, Pierucci S, et al. Chemical Kinetics of Biomass Pyrolysis. Energy Fuels 2008;22:4292–300.
[60] Calonaci M, Grana R, Barker Hemings E, Bozzano G, Dente M, Ranzi E. Comprehensive Kinetic Modeling Study of Bio-oil Formation from Fast Pyrolysis of Biomass. Energy Fuels 2010;24:5727–34.
[61] Eri Q, Peng J, Zhao X. CFD simulation of biomass steam gasification in a fluidized bed based on a multi-composition multi-step kinetic model. Appl Therm Eng 2018;129:1358–68.
[62] Blondeau J, Jeanmart H. Biomass pyrolysis at high temperatures: Prediction of gaseous species yields from an anisotropic particle. Biomass Bioenergy 2012;41:107–21.
[63] Sreejith CC, Muraleedharan C, Arun P. Air–steam gasification of biomass in fluidized bed with CO2 absorption: A kinetic model for performance prediction. Fuel Process Technol 2015;130:197–207.
[64] Font Palma C. Model for Biomass Gasification Including Tar Formation and Evolution. Energy Fuels 2013;27:2693–702.
[65] Shin E-J, Nimlos MR, Evans RJ. A study of the mechanisms of vanillin pyrolysis by mass spectrometry and multivariate analysis. Fuel 2001;80:1689–96.
[66] Ledesma EB, Marsh ND, Sandrowitz AK, Wornat MJ. Global Kinetic Rate Parameters for the Formation of Polycyclic Aromatic Hydrocarbons from the Pyrolyis of Catechol, A Model Compound Representative of Solid Fuel Moieties. Energy Fuels 2002;16:1331–6.
[67] Dorrestijn E, Mulder P. The radical-induced decomposition of 2-methoxyphenol. J Chem Soc, Perkin Transact 1999;2:777–80.
[68] Ranganathan P, Gu S. Computational fluid dynamics modelling of biomass fast pyrolysis in fluidised bed reactors, focusing different kinetic schemes. Bioresour Technol 2016;213:333–41.

[69] Smith B, Loganathan RJM, Shantha MS. A Review of the Water Gas Shift Reaction Kinetics. Int J Chem Reactor Eng 2010;8.
[70] Rhodes C, Hutchings GJ. Studies of the role of the copper promoter in the iron oxide/chromia high temperature water gas shift catalyst. PCCP 2003;5:2719–23.
[71] Plawsky J. Claus Process Reactor Simulation Rensselaer Polytechnic Institute; 2013.
[72] Monnery WD, Hawboldt KA, Pollock A, Svrcek WY. New experimental data and kinetic rate expression for the Claus reaction. Chem Eng Sci 2000;55:5141–8.
[73] Z. S. A Modified Kinetic Reaction Scheme for Claus Reaction Furnaces in Oil Refineries. . Innov Ener Res. 7; 2018.
[74] Hawboldt. K. Kinetic modelling of key reactions in the modified claus plant front end furnace. Hawboldt, K; 1998.
[75] Pahlavan M, Fanaei MA. Modeling and Simulation of Claus Unit Reaction Furnace. Iran J Oil Gas Sci Technol 2016;5:42–52.